Chemical Engineering Journal 446 (2022) 137141

Contents lists available at ScienceDirect

Chemical Engineering Journal

journal homepage: www.elsevier.com/locate/cej

Self-supported hierarchically porous 3D carbon nanofiber network comprising Ni/Co/$NiCo_2O_4$ nanocrystals and hollow N-doped C nanocages as sulfur host for highly reversible Li–S batteries

Rakesh Saroha [a], Young Hoe Seon [a], Bo Jin [b], Yun Chan Kang [c], Dong-Won Kang [d,*], Sang Mun Jeong [e], Jung Sang Cho [a,*]

[a] Department of Engineering Chemistry, Chungbuk National University, Gaesin-Dong, Seowon-Gu, Cheongju 361-763, Republic of Korea
[b] Key Laboratory of Automobile Materials, Ministry of Education, and College of Materials Science and Engineering, Jilin University, Changchun 130022, China
[c] Department of Materials Science and Engineering, Korea University, Anam-Dong, Seongbuk-Gu, Seoul 136-713, Republic of Korea
[d] School of Energy Systems Engineering, Chung-Ang University, 84, Heukseok-Ro, Dongjak-Gu, Seoul 06974, Republic of Korea
[e] Department of Chemical Engineering, Chungbuk National University, Cheongju, Chungbuk 28644, Republic of Korea

ARTICLE INFO

Keywords:
Viable lithium-sulfur batteries
Nitrogen-doped carbon matrices
Porous sulfur hosts
Catholytes
Metal-organic frameworks

ABSTRACT

Hierarchically porous nitrogen-doped carbon nanofibers (P-N-CNF) comprise well-embedded metallic-Ni/Co and spinel-type $NiCo_2O_4$ nanocrystals (Ni-Co/$NiCo_2O_4$) along with metal-organic framework-derived hollow nitrogen-doped carbon nanocages (HNC), denoted as P-N-CNF@NCO/HNC, are rationally designed as cathode substrates for advanced lithium-sulfur batteries with feasible parameters. The highly conductive and porous N-CNF matrix provides numerous conductive channels for rapid ionic and electronic transfer. HNC guarantees efficient impregnation of a large volume of active material along with high loading, channelizing the volume variation stress, and ensuring efficient electrolyte percolation, which is crucial for uniform dispersion and high active sulfur utilization, especially at low electrolyte/sulfur (E/S) ratios. The metallic-Ni/Co and polar spinel-type $NiCo_2O_4$ nanoparticles offer sufficient chemisorption sites to prevent polysulfide migration towards the anode. Li-S cells assembled using P-N-CNF@NCO/HNC as an advanced host and lithium polysulfide catholyte as the starting material displayed stable electrochemical performance even with strident battery parameters, including high sulfur content (79.8 wt%), high sulfur loading (7.7 mg cm^{-2}), and low E/S ratio (8.0 μL mg^{-1}). The cell displays a maximum areal capacity of 5.4 mA h cm^{-2} that stabilizes to 2.8 mA h cm^{-2} after 160 cycles at 0.1 C and is comparable to the theoretical threshold of presently available commercial systems.

1. Introduction

Lithium-sulfur batteries (LSBs) are considered a suitable alternative for the currently available state-of-art lithium-ion battery (LIB) technology, owing to their high theoretical specific discharge capacity (1675 mA h g^{-1}), high gravimetric energy density (2600 Wh kg^{-1}), and relatively high nominal discharge voltage (~2.1 V vs. Li/Li^{+}) [1–4]. Additionally, the natural abundance and environmental friendliness of elemental sulfur result in low processing costs [5,6]. However, the commercialization of LSBs is hindered by several fundamental issues, such as the poor electronic conductivity of sulfur and its end product, the dissolution and migration of intermediate lithium polysulfides (LiPSs) over cycling, and severe volume variations during the charge–discharge process [7–9]. Such issues mostly result in a continuous charging profile, low Coulombic efficiencies, poor active material utilization, substandard rate capabilities, and fast capacity fading during prolonged cycling [10–12]. Furthermore, low active sulfur loading (typically <2 mg cm^{-2}) and high electrolyte/sulfur (E/S) ratio (usually >10 mL g^{-1}) also exaggerate the situation [3,13–18].

To achieve more practically feasible LSBs, the active material loading should be higher than 5 mg cm^{-2} with an E/S ratio not higher than 5 mL g^{-1} [19–21]. Moreover, the areal capacity of the assembled LSBs should be greater than 4 mA h cm^{-2} to outperform the commercially available LIBs [2,22]. However, regular high-loading sulfur electrodes prepared using the traditional slurry casting method are very thick and usually crack and peel off [23]. In addition, thicker electrodes typically result in

---

* Corresponding authors.
E-mail addresses: kangdwn@cau.ac.kr (D.-W. Kang), jscho@cbnu.ac.kr (J.S. Cho).

https://doi.org/10.1016/j.cej.2022.137141
Received 14 March 2022; Received in revised form 3 May 2022; Accepted 20 May 2022
Available online 23 May 2022
1385-8947/© 2022 Elsevier B.V. All rights reserved.

low sulfur utilization due to poor electrode wetting. As a result, most of the active material remains unused; and therefore, the LSB exhibits substandard electrochemical performance. These issues can be readily resolved by using active materials in the liquid phase, usually referred to as a "catholyte," which is formed by mixing elemental S and Li_2S in the desired weight ratio in the bare electrolyte [24–26]. The active sulfur material in the form of a polysulfide solution is dispersed well inside the free-standing substrate. Furthermore, the free-standing nanostructure on the cathode side typically contains highly porous carbon to accommodate the large volume of dissolved lithium polysulfide solution [2]. The high surface area of the porous carbon architecture provides enough space to alleviate the volume stress during repeated cycling and ensures the availability of numerous porous channels for better electrolyte or catholyte penetration to the lowest levels of the substrate. The polyacrylonitrile (PAN)-derived carbon nanofibers (CNFs) as a free-standing framework have always been the first choice of material owing to their ease of synthesis and easily controllable nanostructure, as reported previously [27–30]. Besides, to obtain highly porous CNFs, metal–organic frameworks (MOFs) such as Zn-based zeolitic imidazole framework (ZIF-8, a class of MOFs), play a crucial role as self-sacrificing agents for the development of open mesopores inside the carbon nanostructures [2,31,32]. ZIF-8 consists of central Zn ions connected through organic linkers or imidazolate units. The nitrogen-rich organic linkers converted to nitrogen-doped carbonaceous (N-C) products during the high-temperature heat treatment whereas the volatile Zn species evaporated, leaving highly interconnected hollow nanocages (HNC) in the form of mesopores [2]. The presence of ZIF-8 derived open mesopores allow high active material absorption besides accommodating the severe volume variations during the redox processes. However, the nonpolar nature of PAN and ZIF-8 derived porous carbon offers weak interactions for the chemical adsorption of polar polysulfide solution [1,10]. Therefore, to ensure the efficient prohibition of polysulfide diffusion, the presence of polar host material is highly inevitable.

The numerous polar materials such as metal oxides, chalcogenides, nitrogen-doped carbon, and carbides alongside porous carbon have been studied extensively for the physical and chemical confinement of polysulfides [22,33–39]. However, most reports are based on mono-metal oxides as a polysulfide capturing component [40–43]. In this regard, the introduction of binary transition metal oxides with two different metal cations could be a valuable strategy to enhance polysulfide anchoring and the electronic conductivity of the cathode host because of the coexistence of mixed-valence states in the transition metals [44,45]. The feasibility of using binary transition metal oxides as sulfur hosts has also been reported previously by different research groups [46,47]. For instance, Fan et al. demonstrated the facile synthesis of CNT/$NiFe_2O_4$ nanosheets as sulfur hosts [47]. The obtained CNT-$NiFe_2O_4$-S composite exhibited an initial discharge capacity of 1350 mA h g^{-1} at 0.1 C. In addition, the cycling performance was also noteworthy, with a decay rate of 0.009 % per cycle over 500 cycles at 1.0 C. Likewise, Liu et al. studied S/$NiCo_2O_4$ composites for a high-volumetric-capacity lithium-sulfur battery system and reported a low-capacity fading rate of 0.039 % per cycle at 1.0 C [46]. However, low active material loading (1.0–1.5 mg cm^{-2}), low effective sulfur content in the electrode (49–55 wt%), and high E/S ratio (25–40 μL mg^{-1}) prohibit the commercial pertinence of the above works.

Herein, we introduced a multicomponent 3D freestanding, and porous nitrogen-doped carbon nanofiber (N-CNF) comprising well-embedded metallic-Ni/Co and spinel-type $NiCo_2O_4$ nanoparticles and metal–organic framework-derived hollow nitrogen-doped carbon nanocages (HNC), denoted as P-N-CNF@NCO/HNC, as an advanced cathode substrate for practical LSBs. To obtain a porous structure, zeolitic imidazolate frameworks (ZIF-8) were used as porogens. A conventional electrospinning technique was employed to obtain 1D nanofibers followed by a two-stage heating process to reduce metal precursor salts to their respective metal species and then oxidation to finally obtain spinel-type nickel cobalt oxides well-embedded in the carbon scaffold. A high concentration of dissolved sulfur (5.7 M) in the form of a lithium polysulfide solution (Li_2S_6; 0.95 M) was used to obtain electrodes with high sulfur loading and high effective sulfur content. For general electrochemical performance, lithium-sulfur cells employing a free-standing porous cathode substrate and dissolved lithium polysulfide solution as an active material were assembled with a sulfur loading of 3.6 mg cm^{-2} and effective sulfur content of 64.6 wt% in the cathode. The E/S ratio inside the Li-S cell for typical electrochemical conditions was maintained at 10.9 μL mg^{-1}. Benefitting from the structural merits, enhanced electrochemical performance was obtained even with severe battery parameters such as a high effective sulfur content of 76.7 and 79.8 wt% together with high active material loadings of 5.9 and 7.7 mg cm^{-2}, and low E/S ratio of 8.7, and 8.0 μL mg^{-1}, respectively. Consequently, we surmise that the synergetic effects of synthesizing multicomponent, porous, and conductive nanostructures with well-embedded polar nanoparticles in the present work will provide considerable insights into the progress of advanced free-standing substrates as sustainable cathode hosts.

2. Experimental section

2.1. Chemicals

To synthesize the 3D freestanding porous cathode substrate, analytical grade chemicals were used: polyacrylonitrile (PAN, *Mw* = 150,000, Sigma–Aldrich), 2-methylimidazole (*Mw* = 82.10, 99%, Acros Organics), and zinc nitrate hexahydrate ($Zn(NO_3)_2·6H_2O$; *Mw* = 297.47, 96.0%, Samchun Chemicals), nickel acetate tetrahydrate ($Ni(CH_3COO)_2·4H_2O$; *Mw* = 248.86, 97.0%, Daejung Chemicals & Metals Co., Ltd.), and cobalt acetate tetrahydrate ($Co(CH_3COO)_2·4H_2O$; *Mw* = 249.08, 98.0% purity, Daejung Chemicals & Metals Co., Ltd.). *N, N-dimethylformamide* (DMF, 99.5%, Samchun Chemicals) was used as the solvent to prepare the spinning solution.

2.2. Preparation of cathode substrate

The free-standing porous cathode substrate was visualized using a typical electrospinning technique with subsequent heat treatments. Nanosized ZIF-8 polyhedra were synthesized using a facile solution method, as reported previously [2]. To prepare the electrospinning solution, ZIF-8 polyhedra were added to 20 mL of DMF solvent and ultrasonicated, followed by stirring. This process was repeated until the solution turned milky, with no precipitates. Afterward, stoichiometric amounts of nickel acetate (1.8 mmol), cobalt acetate (3.6 mmol), and PAN (2.0 g) were added to the ZIF-8/DMF solution one by one and allowed to stir at ambient temperature overnight to obtain a homogeneous colloidal suspension. The spinning solution was then loaded into a plastic syringe (12 mL capacity) fitted with a stainless-steel needle (21 gauge). The spinning solution was ejected at a rate of 2 mL h^{-1} onto a rotating drum covered with aluminum foil as a collector. A high voltage of 20 kV was applied between the tip of the needle and the collector, and the distance between the two was fixed at 15 cm. The as-spun PAN/Ni/Co/ZIF-8 composite nanofibers were then stabilized overnight in a hot-air oven maintained at 150 °C. The first heat treatment of the stabilized composite nanofibers was performed at 900 °C in a N_2 atmosphere for 5 h. The composite nanofibers obtained after the first heat treatment were further subjected to a second heat treatment at 300 °C for 2 h in an ambient environment. Finally, 3D free-standing and highly porous nanofibers comprising well-embedded metallic-Ni/Co and spinel-type $NiCo_2O_4$ nanocrystals in addition to hollow N-doped carbon nanocages as a cathode substrate were obtained and are hereafter abbreviated as "P-N-CNF@NCO/HNC." A sample for comparison was also prepared using a spinning solution without ZIF-8 polyhedra. The PAN/Ni/Co composite nanofibers obtained were subjected to a single-step heat treatment at 300 °C for 2 h in air, which resulted in a non-porous or filled-type ("F") morphology hereafter referred to as "F-NCO".

2.3. Physical characterization

The microstructures of the prepared cathode substrates were analyzed using field-emission scanning electron microscopy (FE-SEM; Ultra Plus, Zeiss) and field-emission transmission electron microscopy (FE-TEM; JEM-2100F, JEOL). The phase analysis and crystal structure of the prepared samples were determined using X-ray diffraction (XRD, Bruker, D8 Discover) fitted with Cu $K_{\alpha 1}$ radiation (1.5405 Å) at the Korea Basic Science Institute (Daegu). The chemical environments of various elements in the prepared samples were studied using an X-ray photoelectron spectroscopy (XPS; K-Alpha, Thermo Scientific) instrument equipped with Al Kα radiation. The crystallinity of the carbonaceous products in the nanofibers was analyzed using Raman spectroscopy (LabRam, HR800, Horiba Jobin-Yvon). Adsorption–desorption isotherms were used to measure the surface area and pore volume of the sample with N_2 as the adsorbate gas using the Brunauer–Emmett–Teller (BET) technique. The carbon and nitrogen contents in the nanofibers were quantified using the elemental analysis (EA) technique, whereas the stability of the nanofibers was confirmed using thermogravimetric analysis (TGA, Pyris 1, Perkin Elmer) from room temperature to 700 °C at a heating rate of 10 °C min^{-1} in air or as mentioned otherwise.

2.4. Preparation of catholyte and cell assembly

Before the assembly of Li-S cells, a catholyte was prepared as a liquid active material. Briefly, lithium sulfide (Li_2S; *Mw* = 45.95, Sigma–Aldrich, 99.98%) and elemental sulfur (S, *Mw* = 32.07, Sigma–Aldrich, 99.98%) were mixed in a 5:1 ratio in an appropriate amount of 1.0 M lithium bis-(trifluoromethanesulfonyl) imide in a solvent mixture containing 1,2-dimethoxyethane (DME) and 1,3-dioxolane (DOL) (1:1 v/v) with 0.5 M $LiNO_3$ as the electrolyte additive. A dark brown lithium polysulfide catholyte solution was obtained after stirring the S and Li_2S mixture overnight at 60 °C inside a glove box. The concentration of S was fixed at 5.7 M in the catholyte solution (0.95 M) throughout the experiments. Coin cells were assembled inside a glove box to measure the electrochemical performance of the free-standing and porous cathode substrates. The coin cell comprised P-N-CNF@NCO/HNC@LiPSs as the cathode, metallic lithium discs as the anode, and a polypropylene Celgard membrane as a separator. For standard Li-S cells, 30 μL of 5.7 M polysulfide solution was added to the porous P-N-CNF@NCO/HNC discs (ϕ = 14 mm, average mass = 3.0 mg, average thickness = 202 μm; Fig. S1), which resulted in an effective sulfur content of 64.6 wt% with a sulfur loading of 3.6 mg cm^{-2} (referred to the worked example in the Supporting Information). The electrolyte volume throughout the electrochemical tests was fixed at 30 μL, which resulted in an E/S ratio of 10.9 μL mg^{-1} for the typical Li-S cells. The E/S ratio was calculated according to the total volume of the bare electrolyte and catholyte. Moreover, Li-S cells employing high active material loadings of 5.9 and 7.7 mg cm^{-2} with low E/S ratios of 8.7, and 8.0 μL mg^{-1}, respectively, were also assembled and tested for cycling stability at a particular current-rate value. Notably, the effective sulfur content in the high-sulfur-loading electrodes was fixed at 76.7 and 79.8 wt%, respectively.

2.5. Electrochemical measurements

The assembled Li-S cells were galvanostatically charged and discharged at various C-rates in the voltage window of 1.7–2.8 V. The C-rate was determined by considering the theoretical capacity of 1675 mA h g^{-1} at a C-rate of 1.0. The cyclic voltammetry (CV) curves were obtained at different voltage scan rates ranging from 0.01 to 0.1 mV s^{-1}. All electrochemical measurements were performed using a WBCS3000 battery cycler (WonATech). Impedance spectroscopy (EIS) tests were performed using an electrochemical impedance analyzer workstation (ZIVESP2) in the frequency range of 100 kHz to 10 mHz, with an alternating pulse amplitude of 5 mV.

2.6. Polysulfide adsorption and electrocatalytic measurements

Adsorption experiments to visualize the anchoring of polysulfides and electrocatalytic tests were also performed. Briefly, a LiPS solution (Li_2S_6) in the bare electrolyte of DOL/DME containing 1.0 mol L^{-1} LiTFSI salt was prepared, which contains 2.0 M sulfur in liquid form. The above solution was further diluted to obtain 1.0 mM of Li_2S_6 polysulfide using an appropriate amount of DOL/DME solvent. Two glass vials were then filled with the above polysulfide solution and the prepared samples (5.0 mg each). A polysulfide solution without any sample was prepared as a standard. For electrocatalytic measurements, symmetric cells were assembled using the prepared sample as both the counter and the working electrode (ϕ = 14 mm), with the polysulfide solution (30 μL) filling between the two electrodes. Briefly, the prepared nanofibers were ground with a polyvinylidene fluoride binder and carbon black at a weight ratio of 8:1:1 and dispersed in *N*-methyl-2-pyrrolidone (NMP) as a solvent, followed by coating on an aluminum current collector. The assembled symmetric cells were subjected to CV tests at a scan rate of 3.0 mV s^{-1} in the voltage window of −1.0 to 1.0 V.

3. Results and discussion

3.1. Physical characterization of synthesized materials

Hierarchically porous nitrogen-doped carbon nanofiber scaffolds enabled by multicomponent synergistic effects of well-embedded metallic-Ni/Co and spinel-type $NiCo_2O_4$ nanocrystals along with MOF-derived highly interconnected hollow N-doped C nanocages (P-N-CNF@NCO/HNC) as a self-supported cathode host was synthesized. The comprehensive formation mechanism is shown in Scheme 1. The homogeneous spinning solution comprising a PAN polymer, Co and Ni salt as metal precursors, and ZIF-8 polyhedra (∅ = 70 nm) were electrospun to obtain as-spun PAN/Ni/Co/ZIF-8 composite nanofibers (Scheme 1a-①). The as-spun composite nanofibers were stabilized at 150 °C overnight in a hot air oven, followed by the first heat treatment at 900 °C for 2 h in an N_2 atmosphere. During this process, the PAN matrix was converted to a nitrogen-doped carbon nanofiber (N-CNF) scaffold, whereas the Ni and Co salts were reduced to their respective metallic nanograins well-embedded inside the N-CNF matrix. Moreover, the presence of metallic-Ni/Co nanocrystals resulted in the formation of graphitic carbon from the amorphous carbon surrounding them, owing to their catalytic behavior. Besides, the ZIF-8 polyhedra were disintegrated into a nitrogen-rich organic ligand and a highly volatile Zn/Zn^{2+} species. The nitrogen-rich organic ligand was then converted to nitrogen-doped carbonaceous (N-C) products, whereas the volatile Zn species evaporated, leaving highly interconnected hollow nanocages (HNC), as shown in Scheme 1a-②. Furthermore, the composite nanofibers obtained after the first heat treatment were further subjected to a second heat treatment at 300 °C for 2 h in an ambient environment, which resulted in the partial conversion of well-embedded metallic species to spinel-type $NiCo_2O_4$ nanocrystals (Scheme 1a-③). This facile approach of synthesizing a 3D hierarchically porous cathode substrate that relies on the strategy of utilizing the synergistic effects of multiple components resulted in a self-supported nitrogen-doped carbon nanofiber network with numerous interconnected hollow N-doped carbon nanocages, allowing rapid ionic conduction through the highly conductive N-C scaffold and efficient electrolyte percolation (Scheme 1a-④). To obtain free-standing 3D electrodes, a hierarchically porous and highly conductive P-N-CNF@NCO/HNC sheet was punched into circular discs (∅ = 14 mm) and infiltrated with a highly concentrated lithium polysulfide catholyte as a sulfur source (Scheme 1b). The hollow N-doped carbon nanocages in 3D P-N-CNF@NCO/HNC discs not only acted as reservoirs for high active material absorption but also channeled the large volume variation during the redox processes. Overall, the rationally designed, porous, and highly electronic/ionic conductive nanostructure not only allowed high sulfur loading but also ensured

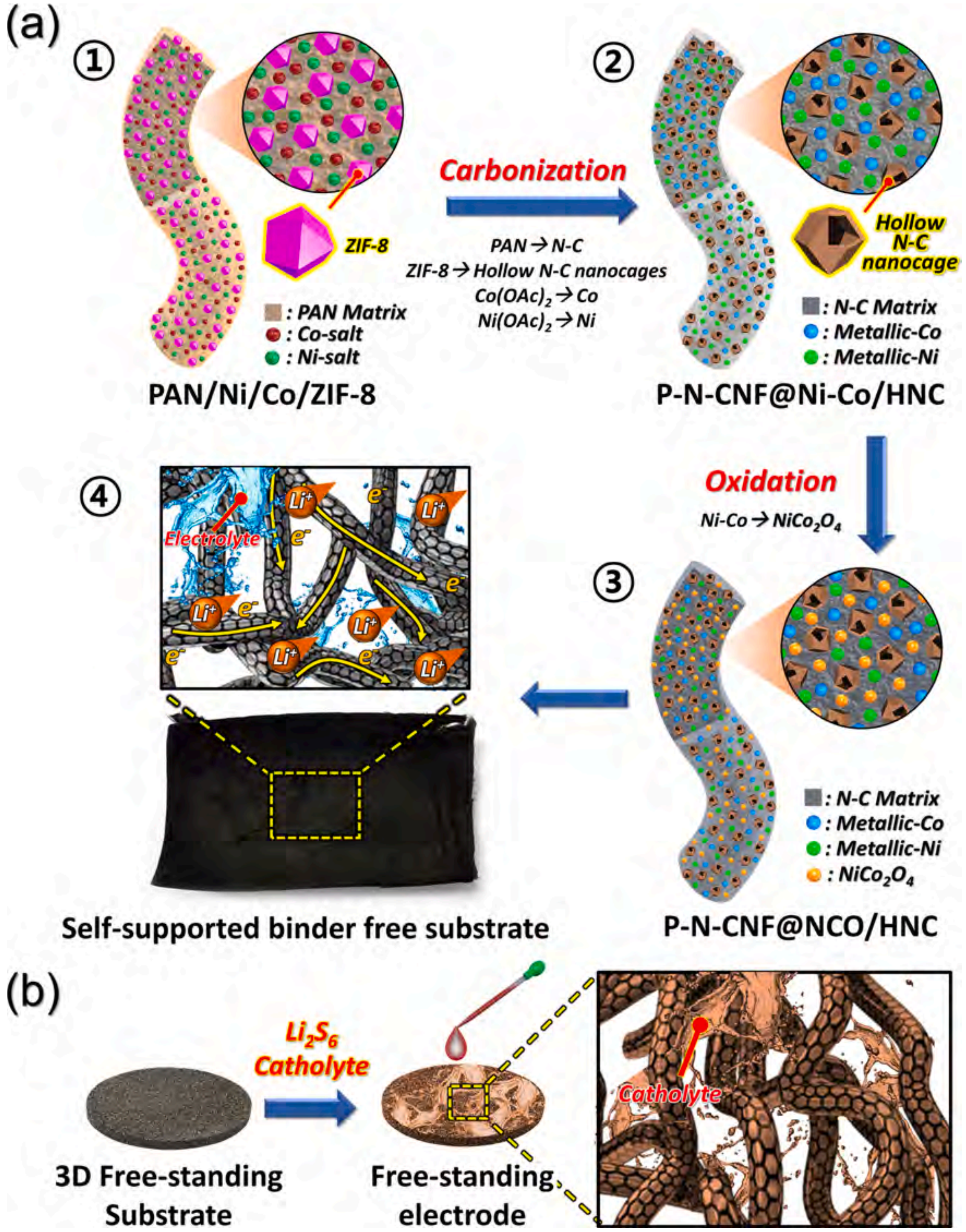

Scheme 1. (a) Schematic representation of (Scheme 1-①,②,③,④) formation mechanism of hierarchically porous and self supported 3D carbon nanofiber network comprising well embedded Ni/Co/NiCo$_2$O$_4$ nanocrystals and hollow N-doped C nancages as advanced cathode host and (b) its applicability as a free-standing 3D electrode for practically viable LSBs.

high active material utilization because of the availability of metallic and polar species. These results envisage the production of a feasible LSB with commercial battery parameters.

To understand the formation mechanism in more detail, we carried out a comprehensive morphological and crystal structure investigation of the nanofibers obtained after each process. The morphologies of the as-spun PAN/Ni/Co/ZIF-8 nanofibers after stabilization at 150 °C are shown in Fig. 1a and b. The FE-SEM micrographs (Fig. 1a) revealed a 1D fibrous morphology with an average diameter of *ca.* 600 nm. In addition, the filled cross-sectional image shown in Fig. 1b suggests a uniform dispersion of the metal precursors and the ZIF-8 polyhedra well inside the nanofibers, as no agglomeration of metal salts and other constituents on the surface of the nanofibers was observed. The XRD pattern of the as-spun nanofibers in Fig. 1c shows intense peaks that are assigned to the ZIF-8 polyhedra only. However, a close examination revealed a broad peak centered at around 2θ = 17°, which corresponds to the PAN polymer, and is flanked by sharp ZIF-8 diffraction peaks on both sides. To confirm this observation, we carried out physical characterization of

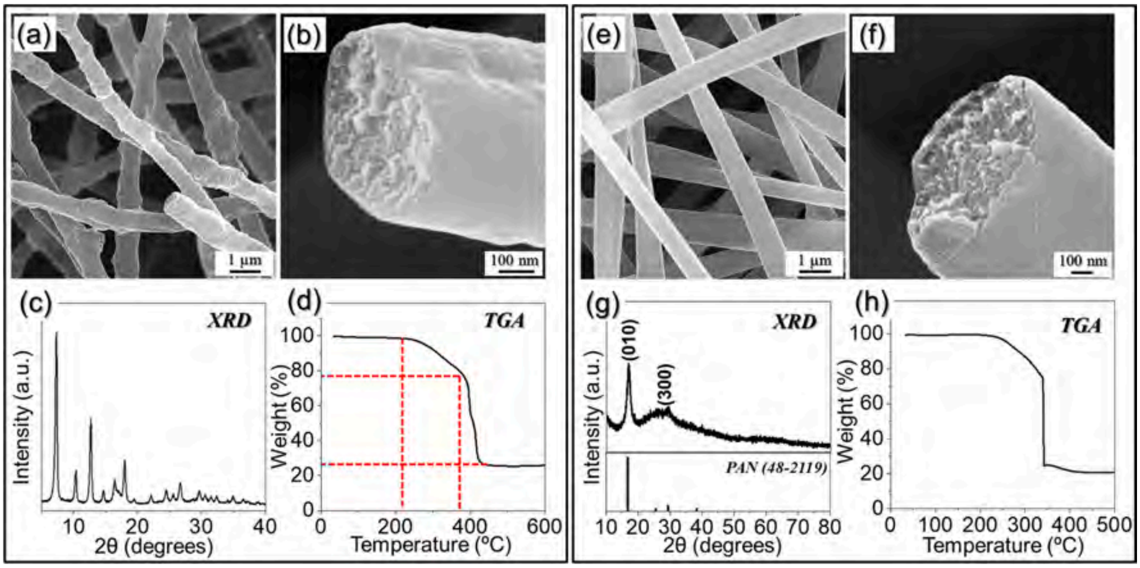

Fig. 1. Morphological, XRD pattern, and TG analysis of (a-d) as-spun PAN/Ni/Co/ZIF-8 and (e-h) as-spun PAN/Ni/Co composite nanofibers obtained after stabilization at 150 °C: (a, e) FE-SEM images, (b, f) cross-sectional images, (c, g) XRD patterns, and (d, h) TG curves.

the as-prepared ZIF-8 polyhedra, as shown in Fig. S2. The FE-SEM micrograph (Fig. S2a) revealed the formation of uniformly sized (*ca.* 70 nm) ZIF-8 polyhedra. The XRD patterns shown in Fig. S2b indicate sharp peaks that could only be attributed to ZIF-8 and are in good agreement with previous reports [48]. As observed, no broad peak at 2θ = 17° was apparent in the XRD pattern of the ZIF-8 polyhedra. Furthermore, TG analysis was carried out using the stabilized nanofibers in an air atmosphere to analyze the thermal stability of the nanofibers. In addition, the TG curve provided information about the optimum oxidation temperature to obtain the pure $NiCo_2O_4$ phase from the precursor salts. As observed, the slight weight loss up to 200 °C was due to the removal of moisture or crystal water from the nanofibers. The first considerable weight loss from 240 to 380 °C could be attributed to the removal of the PAN polymer in the form of CO_2 and the breaking of the metal precursor salts. Afterward, a steeper weight loss from 380 to 430 °C could be attributed to the overall burning of the PAN polymer and the complete conversion of the metal salts to the spinel-type $NiCo_2O_4$ phase, as evidenced by the constant weight after that until 600 °C. For better evaluation, a comparison sample using identical synthesis conditions and technique was prepared without ZIF-8 polyhedra, and the resulting as-spun PAN/Ni/Co composite nanofibers stabilized at 150 °C are shown in Fig. 1(e-h). As observed, the stabilized composite nanofibers display smooth surface fibrous morphology (Fig. 1e) with a uniform dispersion of the metal precursors well inside the nanofibers (Fig. 1f). The XRD pattern in Fig. 1g exhibits diffraction peaks corresponding to the PAN matrix only suggesting the amorphous nature of the nanofibers. The TG analysis curve in Fig. 1h indicates that a phase pure sample can be obtained at around 400 °C.

The hierarchically porous N-C nanofibers comprising well-embedded metallic-Ni and Co species along with hollow N-C nanocages (denoted P-N-CNF/Ni-Co/HNC) were obtained after the first heat treatment of the as-spun PAN/Ni/Co/ZIF-8 composite nanofibers, and the resulting nanofibers are shown in Fig. 2. The nanofibers maintained their 1D fibrous nanostructure (Fig. 2a) even after high-temperature heat treatment with a mean diameter of ~500 nm. Such a high-temperature heating process disintegrates ZIF-8 polyhedra into highly volatile reduced Zn/Zn^{2+} and nitrogen-doped carbonized (N-C) products, in addition to the reduction of metal salts to their respective metallic species. Moreover, the PAN polymer was converted to nitrogen-doped carbonaceous (N-C) materials, which acted as highly conductive scaffold. The reduced Zn/Zn^{2+} species then evaporated, owing to their highly volatile nature, leaving the hollow nanocages surrounded by N-C products, which are mainly carbonized organic linkers. The removal of volatile reduced zinc and the conversion of the PAN polymer to an N-C matrix during the first heat treatment process at a high temperature resulted in shrinkage of the nanofibers. In addition, the presence of hollow N-C nanocages resulted in a highly porous nanostructure, as evidenced by the cross-sectional image shown in Fig. 2b. The well-embedded Ni-Co species in the N-C scaffold, along with the hollow N-C nanocages, are apparent in the TEM images shown in Fig. 2c-f. The dark nanoparticles with a mean size of *ca.* 70 nm are metallic-Ni/Co bonded into a single unit. Furthermore, the gray and bright regions are attributed to the N-C matrix and hollow N-C nanocages, respectively. The HR-TEM image shown in Fig. 2g represents the clear lattice fringe of the N-doped graphitic carbon (NGC) layer and metallic-Co separated by 0.34 nm and 0.20 nm for the (0 0 2) and (1 1 1) crystal planes, respectively. The metallic-Ni/Co acted as a catalyst to effectively convert the amorphous carbon to the graphitic phase during heat treatment. Additionally, the selected area electron diffraction (SAED) pattern (Fig. 2h) and the XRD pattern in Fig. 2i confirm the presence of NGC (broad peak at 2θ = 25°) and metallic-Ni/Co phases in the composite. It should be noted that the almost identical crystal structures of metallic-Ni and Co make it extremely difficult to differentiate their respective crystal planes and XRD peaks. As a result, we surmise that both metallic species were present in the required stoichiometric ratio. This assumption is well supported by the elemental dot mapping results shown in Fig. 2j, which indicates the uniform dispersion of metallic-Ni and Co in the desired proportions along with the elements O, C, and N.

To obtain a hierarchically porous nitrogen-doped carbon (N-C) scaffold comprising well-embedded with metallic-Ni/Co and spinel-type $NiCo_2O_4$ nanocrystals, a second heat treatment was performed, and the resulting nanofibers are shown in Fig. 3. The FE-SEM micrographs (Fig. 3a and b) reveal that the 1D nanostructure of the nanofibers, with an average diameter of 500 nm, remained unchanged. In addition to the intact morphology, open pores were also apparent, as shown in Fig. 3b. The open pores in the final nanostructure result in an efficient electrolyte percolation and enormous ionic/electronic conductive pathways for rapid redox reaction kinetics. Moreover, a porous nanostructure would effectively channel the volume variation during repeated redox processes. The TEM images shown in Fig. 3c-f also reveal the continuous fibrous morphology of the prepared nanofibers with well-embedded spinel-type $NiCo_2O_4$ nanoparticles (ϕ = 70 nm) distributed along the N-C matrix of the nanofiber. However, small traces of nanoparticles with sizes below 50 nm were also observed in the nanofibers, which are

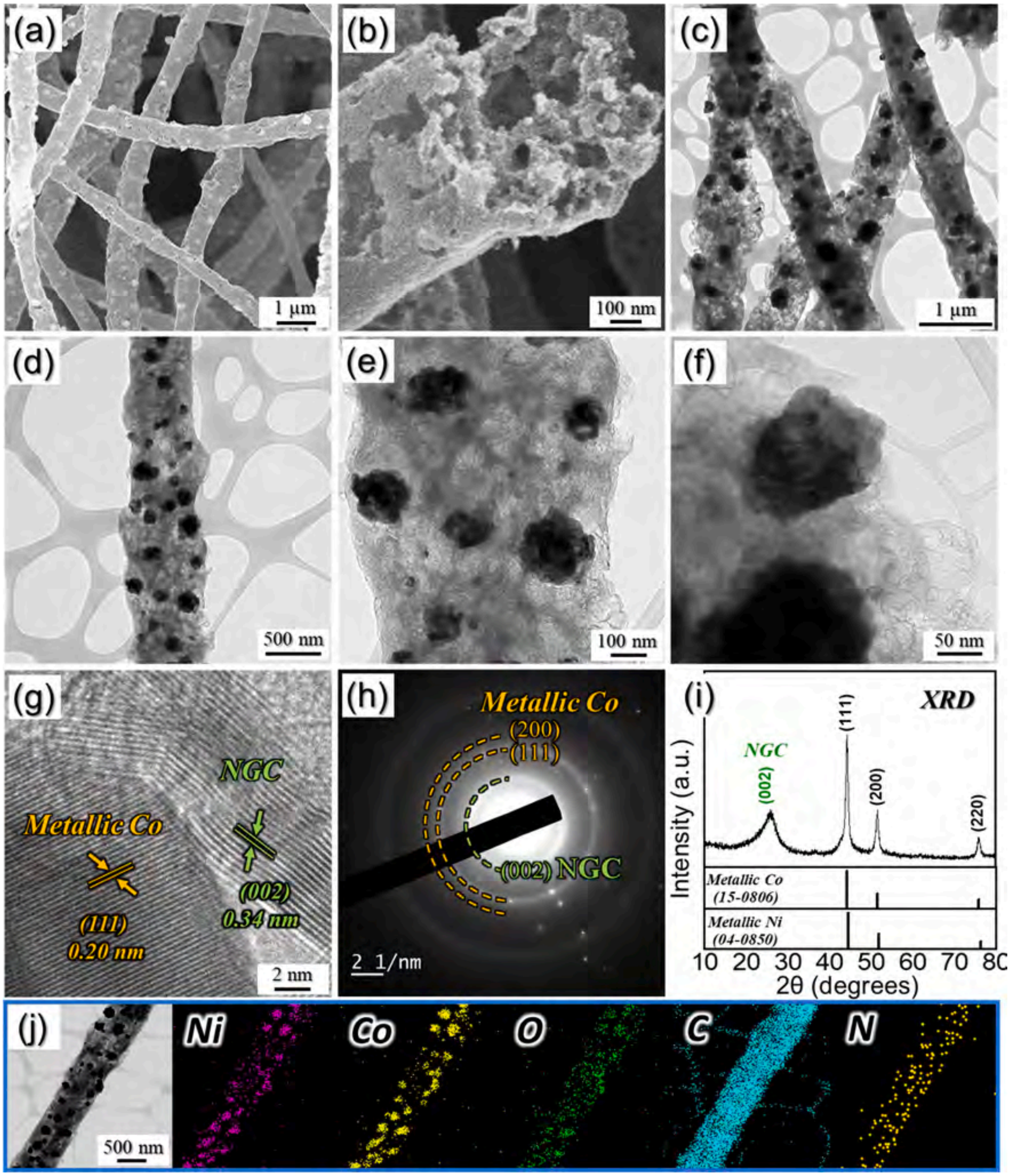

Fig. 2. Characterizations of the P-N-CNF/Ni-Co/HNC composite nanofibers obtained after the first heat-treatment of the as-stabilized nanofibers: (a) FE-SEM image, (b) cross-sectional image, (c-f) TEM images, (g) HR-TEM image, (h) SAED pattern, (i) XRD pattern, and (j) elemental mapping images.

assigned to the metallic-Ni/Co nanocrystals. These observations are in good agreement with the HR-TEM image shown in Fig. 3g, which reveals clear lattice fringes corresponding to the spinel-type $NiCo_2O_4$, metallic-Ni/Co separated by 0.29 nm and 0.20 nm for the crystal planes (2 2 0) and (1 1 1), respectively. The lattice fringe corresponding to the NGC layer separated by 0.34 nm for the crystal plane (0 0 2) was also apparent. The SAED image (Fig. 3h) and the XRD pattern (Fig. 3i) indicate diffraction planes and peaks corresponding to the nanocrystalline $NiCo_2O_4$ (cubic, Fd3m), metallic-Ni/Co, and NGC layers only. Furthermore, the elemental dot mapping images shown in Fig. 3j show the homogeneous distribution of Ni, Co, O, C, and N in the nanofibers. These results suggest that the final nanostructure is a free-standing cathode substrate comprised of a highly conductive NGC matrix, hierarchical porous skeleton due to MOF-derived interconnected hollow N-doped C nanocages, and well-embedded metallic Ni/Co along with spinel-type polar $NiCo_2O_4$ nanoparticles. This combined strategy not only provides enormous conductive channels for fast electronic/ionic transfer in addition to absorbing the severe volume changes but also offers numerous polar sites in the form of embedded Ni-Co/$NiCo_2O_4$ nanocrystals for efficient anchoring and promoting nucleation of the lithium polysulfide species, thus envisages the improved electrochemical performance of the Li-S cell.

The chemical state and bonding environment of the various elements in the free-standing P-N-CNF@NCO/HNC were evaluated using the XPS spectrum, as shown in Fig. 4. The XPS survey spectrum in Fig. 4a indicates photoelectron signals corresponding to the Ni 2p, Co 2p, O 1s, N 1s, and C 1s orbital states. The high-resolution XPS spectrum of Ni 2p shown in Fig. 4b displays well-separated Ni $2p_{3/2}$ and Ni $2p_{1/2}$ peaks at binding energies of 854. 9 and 872.4 eV, respectively, flanked by two satellite peaks (denoted as “Sat.”) at 860.5 and 878.3 eV [49]. In

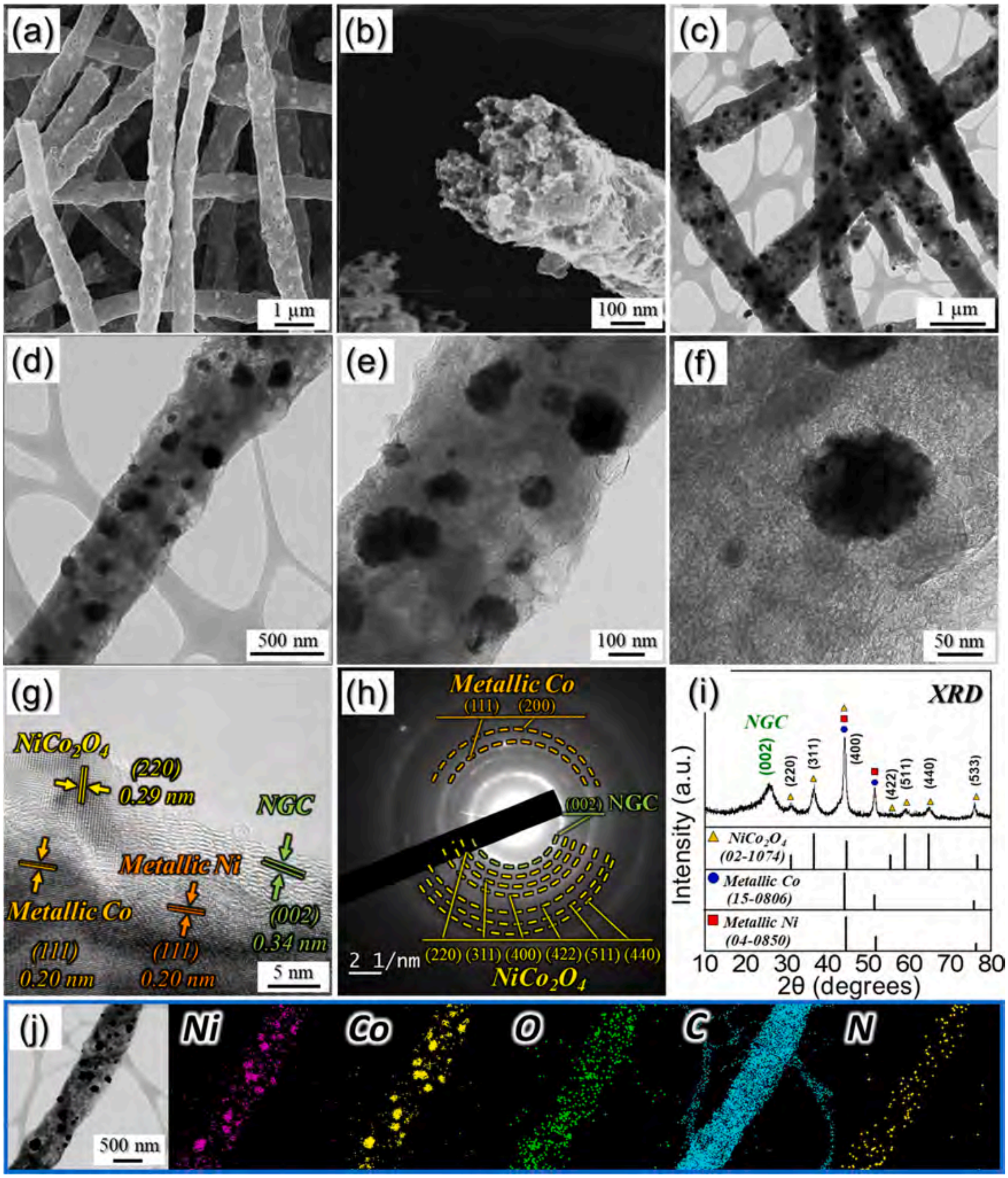

Fig. 3. Characterizations of the P-N-CNF@NCO/HNC composite nanofibers obtained after the second heat-treatment at 300 °C in an air atmosphere: (a) FE-SEM image, (b) cross-sectional image, (c-f) TEM images, (g) HR-TEM image, (h) SAED pattern, (i) XRD pattern, and (j) elemental mapping images.

addition, the deconvolution of Ni $2p_{3/2}$ and Ni $2p_{1/2}$ displays further splitting, suggesting two valence states for Ni, that is, +3 and +2, which matches well with previous reports on $NiCo_2O_4$ [50,51]. In addition, the presence of a peak at a binding energy of 853.2 eV indicates the presence of metallic Ni in the prepared sample. Likewise, the XPS spectrum of Co 2p (Fig. 4c) exhibits two strong peaks, corresponding to Co $2p_{3/2}$ (779.0 eV) and Co $2p_{1/2}$ (794.4 eV). A binding energy difference of 15.4 eV between the two main peaks confirms the spin–orbit splitting, consistent with previous reports [52,53]. Furthermore, the deconvolution of the two main peaks resulted in further splitting, suggesting that the Co cation is both in the divalent and trivalent states [54]. Moreover, the two weak satellite peaks (“Sat.”) at binding energies of 789.0 and 802.8 eV observed distinctly confirms the presence of the Co^{3+} state [52]. The O 1s spectrum shown in Fig. 4d displays three deconvoluted peaks centered at 532.4, 531.0, and 528.8 eV correspond to the adsorbed oxygen molecules near the surface, the O_n^{m-} ions present in the oxygen-deficient regions of $NiCo_2O_4$, and the lattice oxygen present in the spinel-type $NiCo_2O_4$, respectively [52]. The presence of these functional groups is beneficial for the effective capture and catalytic conversion of the polysulfide species. Furthermore, the bonding environment of the carbonaceous material is shown in Fig. 4e, which displays the presence of four photoelectron signals located at 284.0, 285.1, 285.9, and 287.9 eV, corresponding to the $-C{=}C-$, $-C-N-$, $-C-O-$, and $-C{=}O-$ bonds in the nanostructure [55,56]. The high intensity of the $-C{=}C-$ peak confirms the formation of graphitic C in the composite nanofibers. Besides, the presence of the deconvoluted -C-N- peak indicates a nitrogen-doped carbon matrix. In particular, N-doped C offers high electrical conductivity due to the high electronegativity of nitrogen atoms, allowing rapid charge transfer, thus supporting kinetically favored redox reactions. The N 1s deconvoluted spectrum in Fig. 4f

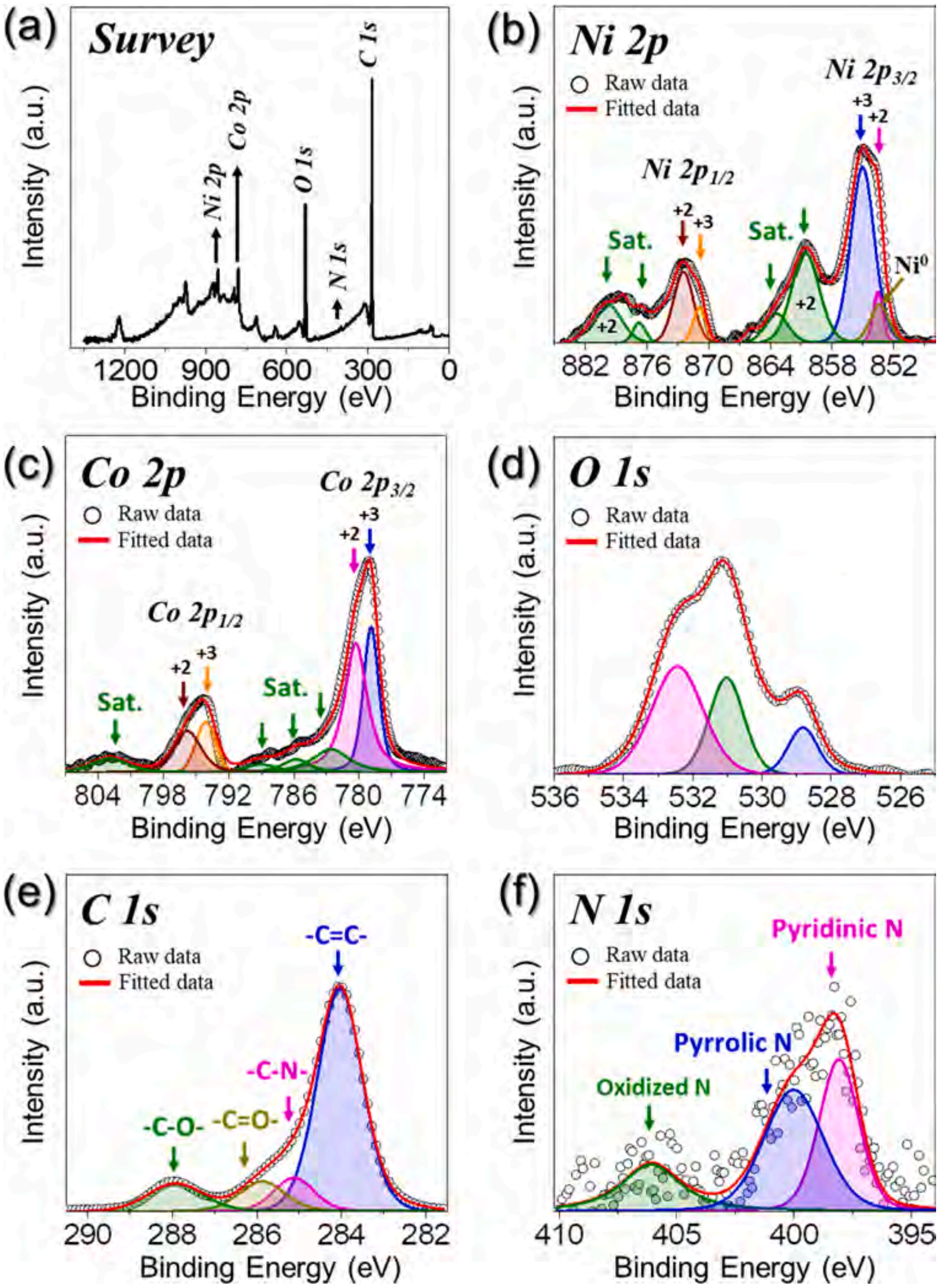

Fig. 4. (a) XPS survey spectrum, (b) deconvoluted Ni 2p XPS spectrum, (c) deconvoluted Co 2p XPS spectrum, (d) deconvoluted O 1s XPS spectrum, (e) deconvoluted C 1s XPS spectrum, and (f) deconvoluted N 1s XPS spectrum.

exhibits three well-fitted peaks, which are attributed to the pyridinic N (398.0 eV), pyrrolic N (400.0 eV), and oxidized N (406.1 eV) species, firmly supporting the -C-N- deconvoluted peak [1]. Overall, the XPS results confirm the presence of $NiCo_2O_4$ nanoparticles with metallic-Ni/Co, which were well embedded inside the N-doped C matrix and eventually allowed fast electrochemical processes.

To further validate the XPS results, TG analysis and Raman spectroscopy were also performed for the P-N-CNF@NCO/HNC nanofibers, as shown in Fig. S3. TG analysis of the prepared nanofibers was performed in air to quantify the carbon content (Fig. S3a) and was *ca.* 51.5 wt%. The obtained value is consistent with the elemental analysis (EA) results shown in Table S1, which estimates the carbon content to 50.2 wt %. In addition, the nitrogen content of 2.4 wt% signifies the nitrogen-doped carbon matrix in the prepared nanofibers. Furthermore, the crystallinity of the carbonaceous material was investigated using Raman spectroscopy, as shown in Fig. S3b. The well-separated peaks at 660.7 and 469.9 cm^{-1} correspond to the A_{1g} and E_g Raman-active modes of the $NiCo_2O_4$ nanostructure, respectively, which arose due to the optical-phonon confinement effect [57]. Additionally, the typical carbonaceous signatures of the D-band (1345 cm^{-1}) and G-band (1580 cm^{-1}) were also observed, whose relative intensity ratio (I_D/I_G) measures the degree of crystallinity of the carbon products [58]. The I_D/I_G ratio of 1.23 indicates that the carbon in the sample mainly consists of disordered carbon with low crystallinity. This could be attributed to nitrogen doping, which produces defects in the carbon framework. Moreover, the defects formed are beneficial in providing surplus insertion sites for Li ions. Furthermore, the porosity of the prepared nanofibers was analyzed using the N_2 adsorption–desorption isotherms shown in Fig. S3c. The existence of a type-IV BET curve with good hysteresis implies the presence of mesopores in the nanostructure that resulted in a high surface area of 280 $m^2\ g^{-1}$ (pore volume = 0.4 $cm^3\ g^{-1}$). In particular, mesopores arose because of the decomposition of the ZIF-8 polyhedra distributed uniformly in the nanofibers (Fig. S3d).

To validate the structural advantages of P-N-CNF@NCO/HNC nanofibers, the as-spun PAN/Ni/Co composite nanofibers stabilized at 150 °C (Fig. 1(e-h)) were subjected to a single-stage heat treatment at 300 °C for 2 h in an air atmosphere, as shown in Fig. S4. The FE-SEM micrographs of the nanofibers with wrinkled surfaces shown in Fig. S4a and b indicate a 1D fibrous morphology with an average diameter of 400 nm. Moreover, the cross-sectional images in Fig. S4b validate the absence of open pores in the structure compared to the P-N-CNF@NCO/HNC nanofibers shown in Fig. 3. The TEM images in Fig. S4c-f confirm the formation of uniformly dispersed $NiCo_2O_4$ nanoparticles (ϕ = 15 nm) well-embedded in the C matrix (dark region) all along the fiber (Fig. S4e and f). In addition, small voids (bright spots) are also evident because of the decomposition of the PAN matrix in air. The HR-TEM images in Fig. S4g firmly authenticate the above results, showing clear lattice fringes with widths of 0.29 nm for the (2 2 0) crystal plane, corresponding to the nanocrystalline spinel-type $NiCo_2O_4$ nanoparticles. The SAED pattern (Fig. S4h) indicates the diffraction rings related to the nanocrystalline phase of $NiCo_2O_4$ only. The XRD pattern (Fig. S4i) shows sharp and intense diffraction peaks which can be attributed to the spinel-type $NiCo_2O_4$ phase, consistent with the above results. The elemental dot mapping results shown in Fig. S4j imply a uniform distribution of Ni, Co, O, and N in the fibrous nanostructure, indicating the formation of a nanocrystalline spinel phase. However, C was sparsely distributed in the fibrous structure, suggesting a relatively low carbon content compared to the P-N-CNF@NCO/HNC nanofibers. The carbon content of the F-NCO sample was determined to be 10.7 wt% from the EA results (Table S1). The chemical states and bonding

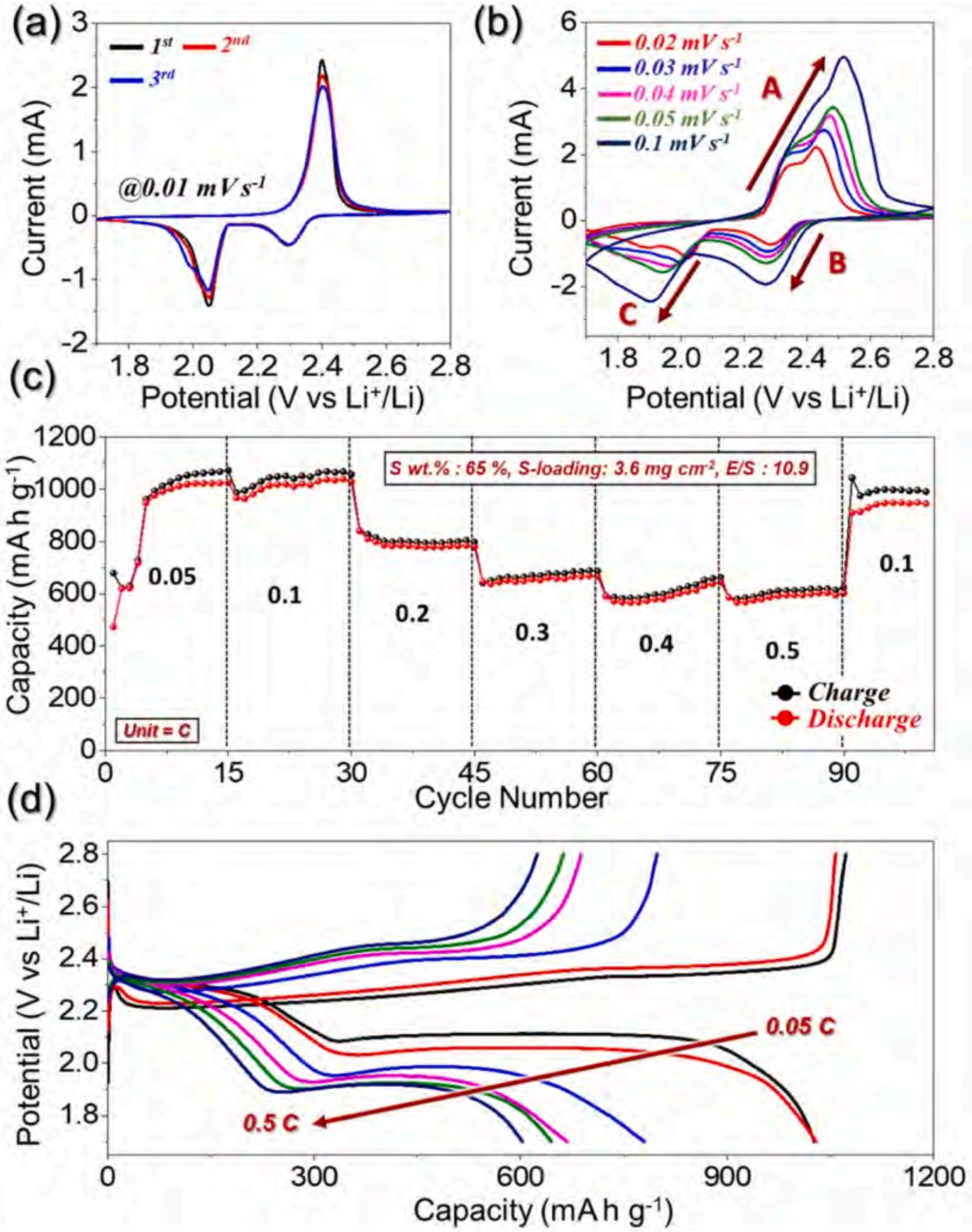

Fig. 5. Electrochemical performance of the Li-S cells utilizing P-N-CNF@NCO/HNC as free-standing cathode substrate and lithium polysulfide (Li_2S_6) catholyte as active material for typical cell parameters: (a) cyclic voltammograms (CV) curves at 0.01 mV s^{-1} for three initial cycles, (b) CV curves at different scan rates ranging from 0.02 to 0.1 mV s^{-1}, (c) rate-capability test at various C-rates (0.05–0.5 C), and (d) respective charge–discharge profiles of the Li-S cell for 15th cycle at different C-rates.

environment of the F-NCO nanofibers obtained using XPS are shown in Fig. S5, showing similar results to those of the P-N-CNF@NCO/HNC sample. The Raman spectra (Fig. S6b) indicate a relatively low-intensity ratio (I_D/I_G) of 1.05, which suggests that the fraction of disordered carbon is relatively low. This is because there are fewer defects in the F-NCO nanofibers compared to P-N-CNF@NCO/HNC. The BET surface area (Fig. S6c) clearly confirms the above results, showing a small surface area of 86 m^2 g^{-1} (pore volume = 0.19 cm^3 g^{-1}) due to the few surface defects in the carbon skeleton. Therefore, the above results suggest that the F-NCO nanofibers mainly comprise uniformly dispersed $NiCo_2O_4$ nanoparticles throughout the nanostructure with low porosity.

3.2. *Electrochemical performance of Li-S cells*

The electrochemical performance of the P-N-CNF@NCO/HNC@LiPS electrode was analyzed to verify its structural merits. The assembled Li-S cells with typical battery parameters were initially subjected to CV tests at various voltage scan rates, as shown in Fig. 5. The three initial CV scans at 0.01 mV s^{-1} shown in Fig. 5a indicate a typical Li-S signature with two cathodic peaks centered at 2.29 and 2.05 V and one sharp anodic peak at 2.40 V. The two cathodic peaks indicate the reduction of more soluble higher-order lithium polysulfides to insoluble lower-order polysulfides, that is, Li_2S through intermediate short order lithium polysulfides [1,2]. During the reverse anodic scan, Li_2S was oxidized to elemental sulfur *via.* intermediate short-order polysulfides and long-order polysulfides, thus completing the redox cycle. In addition, the sharp peaks suggest a kinetically favored redox process, owing to the high electrical conductivity of the N-doped C scaffold, which provides numerous channels for fast ionic/electronic transfer. Likewise, the symmetric and overlapping nature of the CV profiles indicates reversible redox processes due to efficient inhibition of polysulfide diffusion. This is due to the presence of polar spinel-type $NiCo_2O_4$ and metallic-Ni/Co nanoparticles that were well embedded inside the carbon skeleton, providing various polar sites for polysulfide anchoring. These results suggest that the synergistic effects in the P-N-CNF@NCO/HNC cathode substrate guarantee enhanced redox processes owing to the faster ionic/electronic diffusion, better volume stress alleviation, efficient electrolyte percolation, and effective polysulfide immobilization.

Rate capability tests were also performed for the Li-S cells utilizing the P-N-CNF@NCO/HNC@LiPSs electrode, as shown in Fig. 5c. The assembled cells were subjected to charge–discharge processes at various current rates ranging from 0.05 to 0.5 C. The cell displayed an initial discharge capacity of 473 mA h g^{-1} at 0.05 C and steadily increased to 1026 mA h g^{-1} after the 15th cycle, owing to the activation process [59,60]. After that, the cell displayed discharge capacities of 1029, 779, 667, 644, and 602 mA h g^{-1} for the 15th cycle at 0.1, 0.2, 0.3, 0.4, and 0.5 C-rates, respectively. The obtained discharge capacities seem to be feasible considering the high effective sulfur content (65 wt%), high active material loading (3.6 mg cm^{-2}), and low E/S ratio (10.9 μL mg^{-1}). This observation is in accordance with the utilization rate of the active material at different C-rates, as shown in Fig. S7. At low C-rates of 0.05 and 0.1 C, the Li-S cell displayed a high active material utilization of 61 %, which decreased to 36 % capacity utilization at 0.5 C. The better capacity utilization, especially at high C-rates, is attributed to the numerous conductive pathways that result in a rapid charge transfer during the redox processes. Moreover, the presence of polar chemical sites in the form of Ni-Co/$NiCo_2O_4$ nanocrystals effectively prohibits the migration of lithium polysulfide molecules to the anode side. This synergetic effect subsequently resulted in complete redox conversions with no side reactions, as shown in the respective charge–discharge profiles of the assembled Li-S cell in Fig. 5d. The presence of well-distinguished charge–discharge plateaus at all C-rates firmly supports the above reasoning and effectively confirms the structural advantages of the P-N-CNF@NCO/HNC substrate.

To further validate the structural superiority of the prepared porous cathode substrate, the Li-S cell with typical battery parameters was subjected to a cycling performance test at 0.1 C-rate, as shown in Fig. 6a. The cell displayed an initial discharge capacity of 510 mA h g^{-1}, which rapidly increased to 994 mA h g^{-1} at the 10th cycle because of the activation process during cycling. However, the increase in capacity became marginal with further cycling, only displaying a maximum discharge capacity of 1123 mA h g^{-1} at the end of the 75th cycle. The maximum discharge capacity obtained was approximately 67 % of the theoretical capacity (1675 mA h g^{-1}). Furthermore, as cycling proceeded, the cell displayed a slight decrease in discharge capacity, which finally seemed to stabilize at 898 mA h g^{-1} after 220 continuous charge–discharge cycles. In addition, the assembled cell displays a low average capacity decay rate of 0.04 % per cycle (after 10th cycle), considering the practically viable battery parameters. Moreover, the high Coulombic efficiency of 96 % clearly suggests the presence of highly reversible redox reactions. The practical viability of the prepared P-N-CNF@NCO/HNC cathode substrate was also evaluated by considering the areal capacity parameter. As shown in Fig. 6a, the Li-S cell displayed a maximum areal capacity of ~4.0 mA h cm^{-2}, which is almost equal to the theoretical benchmark of the presently available Li-ion systems ($LiCoO_2$ graphite system). Even after long-term cycling, the areal capacity remained as high as 3.2 mA h cm^{-2}, implying the high practical potential of the prepared cathode substrate.

To further broaden the practical applicability, Li-S cells utilizing P-N-CNF@NCO/HNC@LiPS electrodes with severe battery parameters such as high effective sulfur content (~76.7 wt%), high active material loading (5.9 mg cm^{-2}), and low E/S ratio (8.7 μL mg^{-1}) were assembled and cycled at a 0.1 C-rate, as shown in Fig. 6b. The Li-S cell displayed a low initial discharge capacity of 268 mA h g^{-1}, which monotonically increased to 608 mA h g^{-1} for the 35th cycle, indicating activation of the active material over a few initial cycles. With further cycling, the discharge capacity stabilized at 418 mA h g^{-1} after the end of the 400th cycle, indicating an average capacity decay rate of 0.08 % per cycle (considered from the 35th cycle). The decay rate is believed to be reasonable considering the high effective sulfur content, high sulfur loading, and low E/S ratio. In addition, a high Coulombic efficiency of 94 % indicates the excellent reversibility of the redox processes inside the Li-S cell. Additionally, the cell displayed a maximum areal capacity of 3.2 mA h cm^{-2}, which stabilized to 2.5 mA h cm^{-2} after 400 cycles, suggesting that the robust cathode substrate structure allows high active material utilization even at severe battery parameters and prolonged cycling. Benefitting from the structural merits, the effective sulfur content and active material loading were further increased to ~80 wt% and 7.7 mg cm^{-2}, respectively, along with a low E/S ratio of 8.0 μL mg^{-1}. The assembled Li-S cell was subjected to charge–discharge at 0.1 C-rate, shown in Fig. 6c. The cell again displayed similar capacity trends as observed previously, with a low initial discharge capacity of 283 mA h g^{-1}, constantly increased to 687 mA h g^{-1} until the 19th cycle, and then stabilized at 358 mA h g^{-1} after the 160th continuous charge–discharge cycle, with an average capacity decay rate of 0.33 % per cycle. Besides, the cell displayed a maximum areal capacity of 5.4 mA h cm^{-2} that stabilized to 2.8 mA h cm^{-2} after 160 cycles. Furthermore, a stable high Coulombic efficiency of 95 % suggests the remarkable integrity of the electrode. The obtained electrochemical performance in the present work is comparable with that of previous reports, as shown in Table 1. In addition, the contribution of the P-N-CNF@NCO/HNC cathode substrate to the total capacity is negligible except for the first cycle, as shown in Fig. S8. The above electrochemical results firmly suggest that the designed nanostructure of the cathode substrate exceptionally supports a reasonable battery performance even with the harsh parameters. This is due to the synergistic effects of the porous framework, highly conductive channels, and the presence of polar binary metal oxide and metallic-Ni/Co nanocrystals as polysulfide anchoring sites. The above results are more pronounced when considering the gravimetric energy density calculated at the electrode level for Li-S cells utilizing different sulfur loadings and the P-N-CNF@NCO/HNC substrate (Table S2), which again supports the potential of this strategy for practical

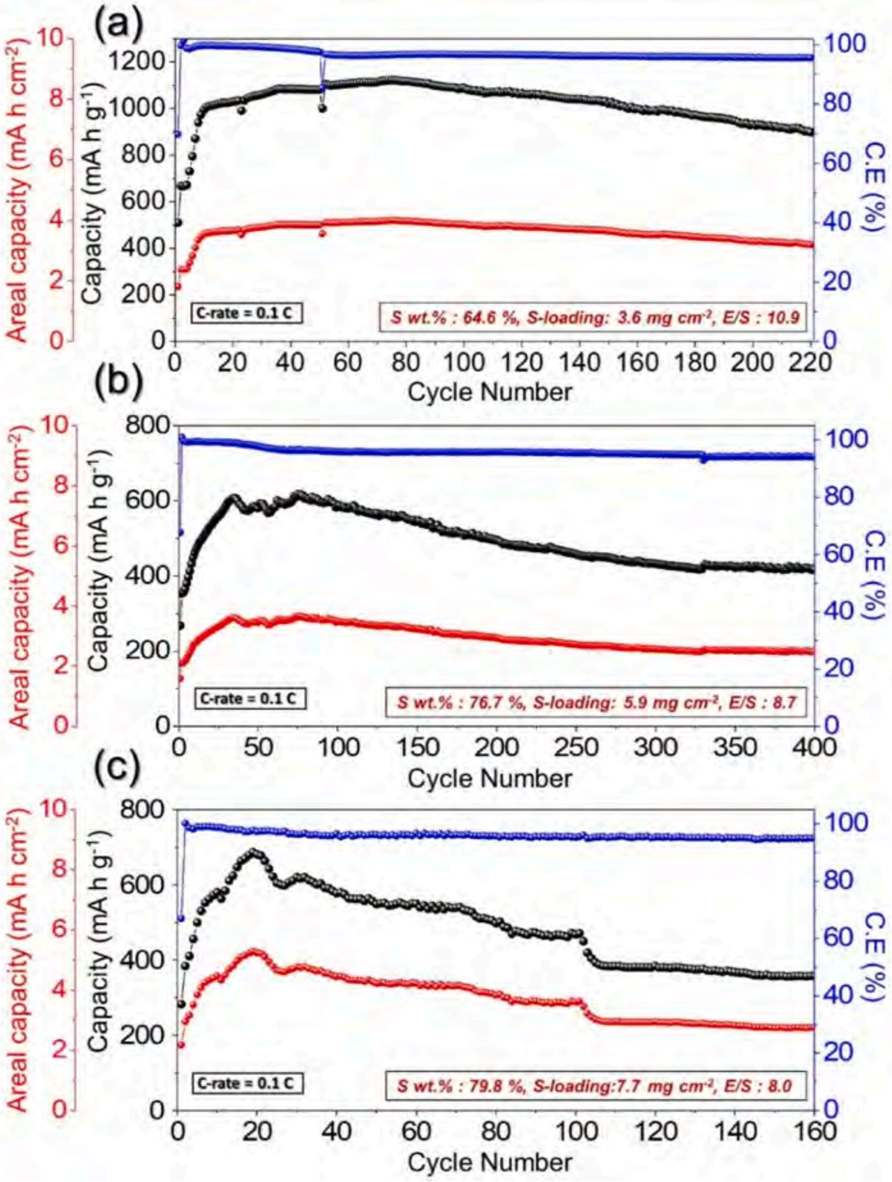

Fig. 6. Cycling performance of the Li-S cells employing free-standing P-N-CNF@NCO/HNC@LiPS electrode with different battery parameters at 0.1 C-rate: (a) typical Li-S cell, and (b, c) Li-S cells with high sulfur content/loading.

applications.

The structural superiority of the P-N-CNF@NCO/HNC cathode substrate was further validated by considering the electrochemical performance of the Li-S cells with non-porous or filled F-NCO@LiPS electrodes, as shown in Fig. S9. The initial CV curves at 0.01 mV s^{-1} of the Li-S cell with typical battery parameters (65 wt% sulfur content, 3.6 mg cm^{-2} sulfur loading, and E/S ratio of 10.9 μL mg^{-1}) displayed somewhat incomplete redox processes, as no obvious cathodic/anodic peaks were observed (Fig. S9a). Instead, asymmetrical and broad peaks were obtained at a low current intensity, suggesting poor charge transfer kinetics during the redox reaction, which subsequently resulted in a large potential polarization. Similar trends were observed for high-voltage scan rates, as shown in Fig. S9b. The high potential polarization clearly implies a sluggish ion diffusion mechanism inside the cell. These observations are supported by the rate capability tests at various current rates (Fig. S9c) and the respective charge–discharge profiles (Fig. S9d). The poor rate capability even at low current rates (0.05 C) validates the above results. In addition, the respective charge–discharge profiles also displayed no obvious plateaus and are in good agreement with the CV results (Fig. S9a). Furthermore, the inferior cycling performance at a 0.1 C-rate (as shown in Fig. S10) for the Li-S cell employing the non-porous F-NCO cathode substrate also suggests sluggish ion kinetics inside the cell. These results unanimously validate the structural merits of the porous P-N-CNF@NCO/HNC cathode substrate, resulting in improved electrochemical results.

The improved electrochemical results of the Li-S cells utilizing different electrodes were further demonstrated using Nyquist plot measurements before and after cycling at 0.1 C in a fully lithiated state, as shown in Fig. S11. The slightly different solution resistance (R_s) values (~12 and 18 Ω before and after cycling, respectively) indicate marginally dissimilar interactions at the electrode–electrolyte interface for the Li-S cell employing the P-N-CNF@NCO/HNC@LiPS electrode, as shown in Fig. S11a. However, a decrease in the total cell resistance from 57 Ω to 5 Ω after 50 continuous charge–discharge cycles suggests superior charge transfer kinetics inside the cell and better electrode integrity. In contrast, the Li-S cell employing the F-NCO@LiPS electrode displayed high resistance values (~2164 Ω) before and after cycling (Fig. S11b), indicating inferior redox reactions inside the Li-S cell. The

Table 1
Electrochemical performance of free-standing P-N-CNF@NCO/HNC cathode substrate with previously reported works based on various battery parameters.

Cathode Substrate	Effective Sulfur (wt.%)	Sulfur Loading (mg cm^{-2})	E/S (μL mg^{-1})	Max. Areal Capacity (mA h cm^{-2})	Max. $C_{discharge}$ / Cycle No. (mA h g^{-1}/-)	Final $C_{discharge}$ /Rate /Cycle No. (mA h g^{-1}/C/-)	Ref.
Highly porous nitrogen-doped carbon nanofiber with embedded nickel cobaltite nanocrystals	**64.6**	**3.6**	**10.9**	**4.0**	**1123/75**	**898/0.1/220**	**This Work**
	76.7	**5.9**	**8.7**	**3.2**	**608/35**	**418//0.1/400**	
	79.8	**7.7**	**8.0**	**5.4**	**687/19**	**358/0.1/160**	
3D-integrated hollow carbon fiber foam	57	6.2	60*	6.4	1263/1	1050/0.1/50	[15]
Nitrogen-rich carbon fiber	–	–	10*	–	1442/10	1278/0.1/60	[61]
Molybdenum carbide embedded carbon nanofiber	–	4.74#	15	–	977/0.2	828/0.2/250	[62]
Carbon nanofiber coated Co_3S_4 nanosheets	–	1.7	15.6	1.5	710/1	710/1.0/200	[63]
		6.8	7.8	4.1	375/1	592/0.1/100	
Nitrogen-doped carbon nanofiber	–	3.08	20	–	967/1	773/0.2/150	[64]
Nanoflower-like MnO_2-kb@carbon paper	–	2.1	–	–	776/1	814/0.5/100	[65]
SnS_2-nanodots@graphene	75	2.5	10	5.0	1234/0.2	1016/0.2/300	[66]
ACNF/Co_3S_4/S paper electrode	50–55	2.5	–	–	953/1	610/1.0/450	[67]
		7.5		5.25	950/1	701/0.3/100	
		13.5		7.0	957/1	550/0.3/100	
Binder-free Carbon Nanofiber	–	6.5	52*	3.5	880/1	700/1.0/80$	[68]
CNT-CNF freestanding cathode	60	16	15	7.1	771/1	480/0.1/100	[69]
Carbonized sucrose-coated eggshell membranes	–	3.2	–	–	1327/1	1000/0.1/100	[70]
Carbon nanofiber sponges	40	–	–	–	688/125	598/0.5/300	[71]
3D sponge-like carbon nanotube	56	2	–	–	767/1	613/0.5/800	[72]
3D r-GO aerogel	–	3.3	–	2.8	–	–	[73]
Nitrogen-doped rGO/CNT hybrid aerogel	–	6	–	–	1100/1	610/0.5/400	[74]
MWCNT-paper	62	1.7	40*	–	1261/1	1179/0.5/50	[75]
PEI-GC aerogel	–	6	–	5.8	1125/1	950/2.0/100$	[76]
		10		6.0	1072/1	590/1.68/50$	
		18		12.0	1079/1	671/1.25/30$	
WS_2-rGO-CNT aerogel	–	3.84	–	4.0	1100/1	860/0.5/100	[77]
Free-standing nitrogen-doped graphene paper	66	1.06	20*	–	1300/20	1100/0.2/100	[78]
MOF-derived N-doped carbonaceous composite	–	2.03	–	–	926/4	766/0.5/250	[79]
		5.10	13.89	4.69	–	–	

'#' Sulfur-loading is in mg; '*' Electrolyte volume is in μL; '**$**' C-rate is in mA cm^{-2}.

above results firmly support the overall improved electrochemical performance of the P-N-CNF@NCO/HNC cathode substrate, which was primarily developed because of its structural superiority.

The structural superiority of the P-N-CNF@NCO/HNC and its capability to suppress polysulfide diffusion was further validated using electrocatalytic activity tests and polysulfide adsorption experiments, as shown in Fig. 7. Symmetric cells were assembled using P-N-CNF@NCO/HNC and F-NCO samples as both working and counter electrodes and filled in between with 20 μL of 1.0 mM Li_2S_6 polysulfide solution. The CV tests recorded for the initial five cycles at a voltage scan rate of 3 mV s^{-1} in the voltage range of –1.0 to +1.0 V are shown in Fig. 7a-c. The first CV scan in Fig. 7a indicates that the pristine F-NCO sample displayed poor electrocatalytic activity towards lithium polysulfide, evident from the widely spaced broad redox peaks accompanied by low current values. In contrast, the symmetric cell utilizing P-N-CNF@NCO/HNC electrodes displayed well-distinguished and relatively sharp redox peaks along with high current values, indicating excellent electrocatalytic activity towards lithium polysulfide. Moreover, the exactly symmetric and overlapping CV profile of the P-N-CNF@NCO/HNC electrodes over repeated cycling (Fig. 7b) compared to the pristine F-NCO electrodes (Fig. 7c) confirms the above results. These results were further validated through a visual demonstration of polysulfide adsorption by the two samples, as shown in Fig. 7d. The digital photographs taken over different time intervals indicate a concomitant color change from yellow ($t = 0$) to almost colorless ($t = 1$ h) for the P-N-CNF@NCO/HNC sample compared to the pristine F-NCO sample. This indicates efficient polysulfide immobilization, which can be attributed to the presence of metallic-Ni/Co and polar spinel-type $NiCo_2O_4$ nanoparticles, which acted as polar sites for the chemical adsorption of lithium polysulfide. Therefore, the above results confirm the structural merits of the P-N-CNF@NCO/HNC cathode substrate, which not only guarantees high structural integrity even at harsh battery parameters but also offers efficient polysulfide capture during prolonged cycling, and hence, superior electrochemical performance. Likewise, Li-S cells with different sulfur loading values of 5.9 and 7.7 mg cm^{-2} were connected in series to power an external load (a 5 V, 10 mW light-emitting diode) after cycling at a 0.1 C-rate, as shown in Fig. 7e. The series cell combination provided a continuous power supply to the load for 30 m and thus validates all the electrochemical results discussed above.

3.3. *Investigation of cycles Li-S cells:*

The structural stability of the P-N-CNF@NCO/HNC cathode substrate was further examined via post-cycling morphological analysis, as shown in Fig. 7(f-i). The Li-S cell utilizing the P-N-CNF@NCO/HNC substrate with a sulfur loading of 7.7 mg cm^{-2} was disassembled carefully inside the glovebox after cycling at 0.1 C followed by drying the electrode to remove the solvent. Likewise, the Li-S cell employing the F-NCO cathode host was dismantled and the different cell parts were collected. The FE-SEM micrographs of the P-N-CNF@NCO/HNC@LiPS electrode (Fig. 7f) revealed that even with a high sulfur content and loading, the fibrous morphology was well-maintained. However, the fiber nanostructure was completely filled with a high volume of catholyte, suggesting complete absorption of the liquid active material. In contrast, the F-NCO electrode (Fig. 7g) displayed large deposits of unused active material throughout the nanofibers, owing to its highly non-porous structure. This observation strongly suggests that the porous structure in P-N-CNF@NCO/HNC not only provides hollow reservoirs for high active material absorption but also effectively channels off the volume stress during cycling. In addition, efficient electrolyte percolation ensures better utilization of the active material and, hence, superior electrochemical performance. These results are further supported by the digital photographs of the Celgard obtained after cycling. The Celgard used with the P-N-CNF@NCO/HNC@LiPS electrode (Fig. 7h) displayed a yellowish color compared to the Celgard used with the F-NCO@LiPS electrode, which revealed dark brown deposits, in accordance with the

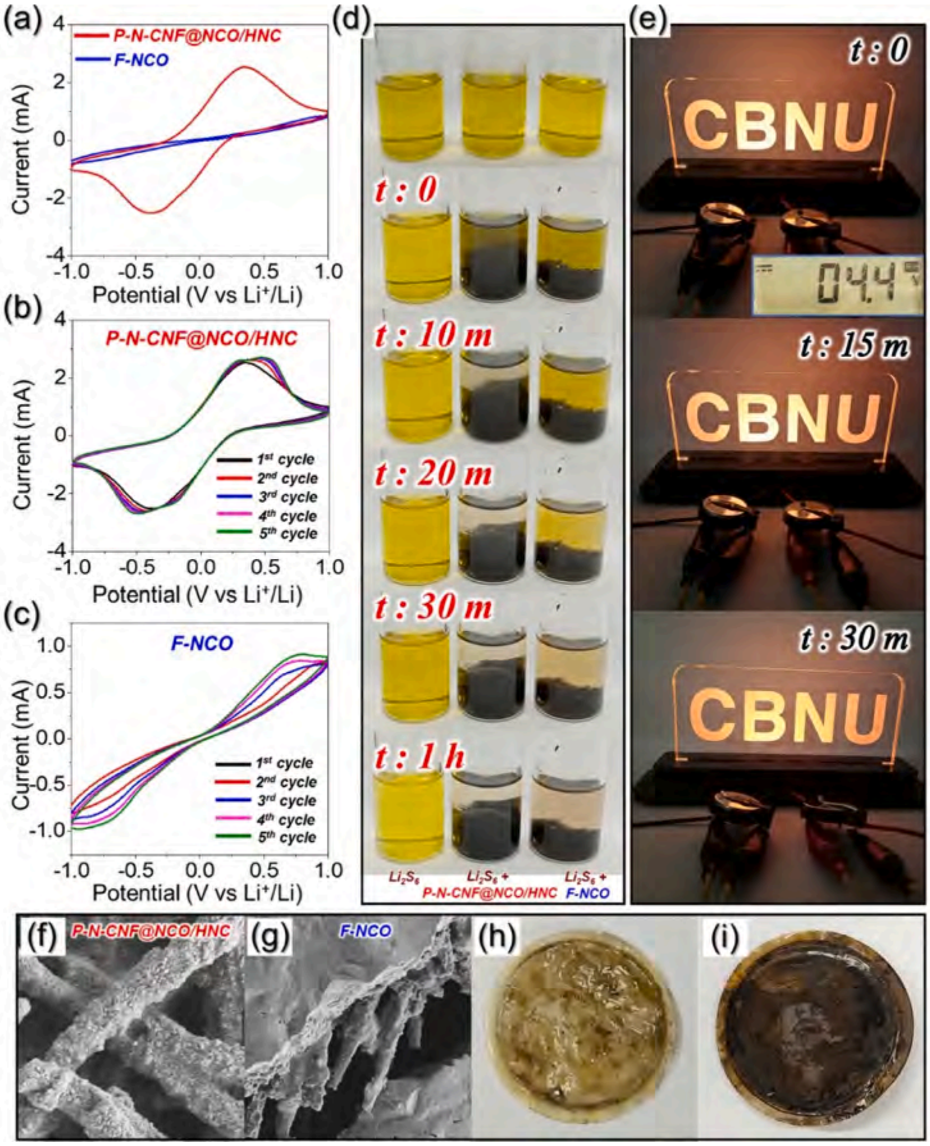

Fig. 7. Electrocatalytic activity and adsorption tests of lithium polysulfides using free-standing P-N-CNF@NCO/HNC and F-NCO cathode substrate: (a) Initial CV curves for different symmetric cells obtained at 3.0 mV s^{-1} in the voltage range of −1.0 to 1.0 V, (b) Five initial CV cycles for symmetric cell employing P-N-CNF@NCO/HNC, (c) Five initial CV cycles for symmetric cell employing F-NCO, and (d) digital photographs of the lithium polysulfide adsorption test at different span of time, (e) digital photographs of a light-emitting diode (5 V, 10 mW) powered by series combination of two Li-S cells with sulfur loadings of 5.9 and 7.7 mg cm^{-2} after cycling at 0.1 C-rate, anode facing-side FE-SEM images of the free-standing cycled electrode along with the digital photographs of the Celgard separator after cycling at 0.1 C-rate: (f, h) P-N-CNF@HNC/NCO, and (g, i) F-NCO.

cycled morphology of the electrode (Fig. 7i). Therefore, the above results confirm that the porous structure of the P-N-CNF@NCO/HNC substrate confined the active material species within the cathodic region, whereas the NCO nanocrystals offered chemisorption sites for polysulfide anchoring. This synergetic effect resulted in higher active material utilization, better mitigation of polysulfide diffusion, and efficient electrolyte percolation. Elemental dot mapping results were also obtained for the two cycled electrodes, as shown in Fig. S12a and b, which revealed that a high fraction of sulfur species in the F-NCO substrate (12.5 wt%) remained unutilized compared to that in the P-N-CNF@NCO/HNC (7.2 wt%). These results are in good agreement with the FE-SEM micrographs of the cycled lithium anode shown in Fig. S13. The lithium anode employed in the Li-S cell utilizing the P-N-CNF@NCO/HNC cathode substrate displayed a much smoother surface with no crack formation (Fig. S13a) compared to the cell employing the F-NCO substrate, which displayed a highly disintegrated lithium surface morphology (Fig. S13b). In addition, elemental dot mapping and the EDS spectra revealed a low diffusion of sulfur-like species towards the anode side for the P-N-CNF@NCO/HNC substrate than the F-NCO substrate, which shows large polysulfide deposits over the metallic anode. These results were further supplemented by observing the changes in the XPS profiles of various elements after cycling, as shown in Fig. S14. The XPS signals for Ni 2p and Co 2p core levels after cycling (Fig. S14a; bottom panel) exhibit a slight shift in binding energy values along with a significant decrease in the fraction of Ni^{3+} and Co^{3+}, as evident from the decrease in peak intensity. This indicates that both Ni^{3+} and Co^{3+} get partially reduced due to the charge transfer from the S_n^{2-} species in the Li_2S_6 catholyte [46]. Additionally, the S 2p spectra was also observed for cycled electrodes in Fig. S14b. The deconvoluted XPS profiles exhibit well-fitted peaks at binding energies of 168.7, 166.7, 163.4, and 160.7 eV that corresponds to the polythionate complex, thiosulfate, bridging sulfur (S_B^0) of Li_2S_6, and S-Ni/S-Co species [46,80]. Thus formed polythionate species act a mediator to weaken the shuttling effect through chemical interaction with lithium polysulfide species [81,82]. These results again validate the efficient anchoring of polysulfides or sulfur-like species by the P-N-CNF@NCO/HNC substrate, in addition to providing sufficient space for high active material volume intake, sufficient space to absorb volume stress, and superior electrolyte infiltration. The above results clearly validate that synthesizing a cathode host with a highly porous morphology, conductive channels, and the presence of polar species produces synergistic effects that result in enhanced electrochemical performance. Moreover, the synthesis and electrochemical results presented in this work would surely help in the advancement of tailoring novel materials for energy and related applications that are based on various chemical processes or chemical engineering techniques.

4. Conclusions

In summary, we proposed a porous and highly conductive 3D free-standing cathode substrate for advanced LSBs based on feasible operating parameters. The advanced cathode substrate primarily comprises a highly conductive N-CNF scaffold with well-embedded metallic-Ni/Co and spinel-type $NiCo_2O_4$ nanocrystals and metal–organic framework-derived HNCs. The highly porous and conductive N-CNF framework guarantees high active material absorption, provides enough space to channelize the severe volume stress during prolonged cycling, efficient electrolyte penetration for fast ion diffusion processes, and enormous conductive channels for rapid charge transfer to support redox kinetics. In addition, the presence of numerous chemisorption sites in the form of metallic-Ni/Co and polar spinel-type $NiCo_2O_4$ nanocrystals ensured effective polysulfide anchoring, thus enhancing active material utilization. Benefitting from the synergistic effects of the conductive and porous nanostructure design, LSBs employing P-N-CNF@NCO/HNC as the cathode substrate and highly concentrated lithium polysulfide solution (Li_2S_6; 0.95 M) as the starting active material, displayed stable electrochemical performance even with viable battery parameters such as super-high sulfur content (79.8 wt%), high sulfur loading (7.7 mg cm^{-2}), and low E/S ratio (8.0 μL mg^{-1}). Overall, we believe that the nanostructure design strategy presented in this work will provide considerable insights into the progress of advanced free-standing substrates as sustainable electrodes for various energy storage applications.

Declaration of Competing Interest

The authors declare that they have no known competing financial interests or personal relationships that could have appeared to influence the work reported in this paper.

Acknowledgements

This work was supported by a National Research Foundation of Korea (NRF) grant funded by the Korean government (MSIP) (NRF-2021R1A4A2001687, and NRF-2021R1I1A3057700) and Chungbuk National University BK21 program (2021).

Appendix A. Supplementary data

Supplementary data to this article can be found online at https://doi.org/10.1016/j.cej.2022.137141.

References

[1] R. Saroha, J.H. Oh, J.S. Lee, Y.C. Kang, S.M. Jeong, D.-W. Kang, C. Cho, J.S. Cho, Hierarchically porous nanofibers comprising multiple core–shell Co_3O_4@graphitic carbon nanoparticles grafted within N-doped CNTs as functional interlayers for excellent Li–S batteries, Chem. Eng. J. 426 (2021), 130805.

[2] R. Saroha, J.H. Oh, Y.H. Seon, Y.C. Kang, J.S. Lee, J.S. Cho, Freestanding interlayers for Li–S batteries: design and synthesis of hierarchically porous N-doped C nanofibers comprising vanadium nitride quantum dots and MOF-derived hollow N-doped C nanocages, J. Mater. Chem. A 9 (2021) 11651–11664.

[3] R. Saroha, J.-H. Ahn, J.S. Cho, A short review on dissolved lithium polysulfide catholytes for advanced lithium-sulfur batteries, Korean J. Chem. Eng. 38 (3) (2021) 461–474.

[4] Y.H. Seon, R. Saroha, J.S. Cho, Hierarchically porous N-doped C nanofibers comprising TiO_2 quantum dots and ZIF-8-derived hollow C nanocages as ultralight interlayer for stable Li–S batteries, Compos. B. Eng. 237 (2022), 109856.

[5] S. Yang, Q. Liu, Q. Lu, E. Zhang, U.S. Arrozi, H. Li, S. Kaskel, F. Xu, H. Wang, A Facile strategy to improve the electrochemical performance of porous organic polymer-based lithium–sulfur batteries, Energy Technol. 7 (2019) 1900583.

[6] Z. Cheng, H. Pan, H. Zhong, Z. Xiao, X. Li, R. Wang, Porous organic polymers for polysulfide trapping in lithium–sulfur batteries, Adv. Funct. Mater. 28 (2018) 1707597.

[7] S. Li, B.o. Jin, X. Zhai, H. Li, Q. Jiang, Review of carbon materials for lithium-sulfur batteries, ChemistrySelect 3 (8) (2018) 2245–2260.

[8] T. Ali, C. Yan, 2 D materials for inhibiting the shuttle effect in advanced lithium–sulfur batteries, ChemSusChem 13 (6) (2020) 1447–1479.

[9] Y. Yang, Y. Zhong, Q. Shi, Z. Wang, K. Sun, H. Wang, Electrocatalysis in lithium sulfur batteries under lean electrolyte conditions, Angew. Chem. 130 (47) (2018) 15775–15778.

[10] R. Saroha, J. Heo, X. Li, N. Angulakshmi, Y. Lee, H.-J. Ahn, J.-H. Ahn, J.-H. Kim, Asymmetric separator integrated with ferroelectric-$BaTiO_3$ and mesoporous-CNT for the reutilization of soluble polysulfide in lithium-sulfur batteries, J. Alloys Compd. 893 (2022), 162272.

[11] G. Xu, Q.-b. Yan, P. Bai, H. Dou, P. Nie, X. Zhang, Nano-sized titanium nitride functionalized separator improves cycling performance of lithium sulfur batteries, ChemistrySelect 4 (2) (2019) 698–704.

[12] D.-G. Wang, L. Tan, H. Wang, M. Song, J. Wang, G.-C. Kuang, Multiple covalent triazine frameworks with strong polysulfide chemisorption for enhanced lithium-sulfur batteries, ChemElectroChem 6 (10) (2019) 2777–2781.

[13] S. Lu, Y. Chen, X. Wu, Z. Wang, Y. Li, Three-dimensional sulfur/graphene multifunctional hybrid sponges for lithium-sulfur batteries with large areal mass loading, Sci. Rep. 4 (2014) 1–4.

[14] Z.-L. Xu, J.-K. Kim, K. Kang, Carbon nanomaterials for advanced lithium sulfur batteries, Nano Today 19 (2018) 84–107.

[15] R. Fang, S. Zhao, P. Hou, M. Cheng, S. Wang, H.-M. Cheng, C. Liu, F. Li, 3D interconnected electrode materials with ultrahigh areal sulfur loading for Li–S batteries, Adv. Mater. 28 (17) (2016) 3374–3382.

[16] H.J. Peng, J.Q. Huang, X.B. Cheng, Q. Zhang, Review on high-loading and high-energy lithium–sulfur batteries, Adv. Energy Mater. 7 (2017) 1700260.

[17] R. Xu, J. Lu, K. Amine, Progress in mechanistic understanding and characterization techniques of Li-S batteries, Adv. Energy Mater. 5 (2015) 1500408.

[18] R. Saroha, J.S. Cho, Nanofibers comprising interconnected chain-like hollow N-doped C nanocages as 3D free-standing cathodes for Li–S batteries with super-high sulfur content and lean electrolyte/sulfur ratio, Small Methods 6 (5) (2022) 2200049.

[19] M. Hagen, D. Hanselmann, K. Ahlbrecht, R. Maça, D. Gerber, J. Tübke, Lithium–sulfur cells: the gap between the state-of-the-art and the requirements for high energy battery cells, Adv. Energy Mater. 5 (2015) 1401986.

[20] M.A. Pope, I.A. Aksay, Structural design of cathodes for Li-S batteries, Adv. Energy Mater. 5 (2015) 1500124.

[21] D. Eroglu, K.R. Zavadil, K.G. Gallagher, Critical link between materials chemistry and cell-level design for high energy density and low cost lithium-sulfur transportation battery, J. Electrochem. Soc. 162 (6) (2015) A982–A990.

[22] J. Song, T. Xu, M.L. Gordin, P. Zhu, D. Lv, Y.-B. Jiang, Y. Chen, Y. Duan, D. Wang, Nitrogen-doped mesoporous carbon promoted chemical adsorption of sulfur and fabrication of high-areal-capacity sulfur cathode with exceptional cycling stability for lithium-sulfur batteries, Adv. Funct. Mater. 24 (9) (2014) 1243–1250.

[23] L. Qie, C. Zu, A. Manthiram, A high energy lithium-sulfur battery with ultrahigh-loading lithium polysulfide cathode and its failure mechanism, Adv. Energy Mater. 6 (2016) 1502459.

[24] R. Demir-Cakan, M. Morcrette, A. Guéguen, R. Dedryvère, J.-M. Tarascon, Li–S batteries: simple approaches for superior performance, Energy Environ. Sci. 6 (2013) 176–182.

[25] S.S. Zhang, J.A. Read, A new direction for the performance improvement of rechargeable lithium/sulfur batteries, J. Power Sources 200 (2012) 77–82.

[26] Y. Yang, G. Zheng, Y. Cui, A membrane-free lithium/polysulfide semi-liquid battery for large-scale energy storage, Energy Environ. Sci. 6 (2013) 1552–1558.

[27] X. Zhou, Y. Wang, C. Gong, B. Liu, G. Wei, Production, structural design, functional control, and broad applications of carbon nanofiber-based nanomaterials: a comprehensive review, Chem. Eng. J. 402 (2020), 126189.

[28] M. Inagaki, Y. Yang, F. Kang, Carbon nanofibers prepared via electrospinning, Adv. Mater. 24 (19) (2012) 2547–2566.

[29] S.-H. Yoon, S. Lim, Y. Song, Y. Ota, W. Qiao, A. Tanaka, I. Mochida, KOH activation of carbon nanofibers, Carbon 42 (8-9) (2004) 1723–1729.

[30] X. Zhou, B. Liu, Y. Chen, L. Guo, G. Wei, Carbon nanofiber-based three-dimensional nanomaterials for energy and environmental applications, Mater. Adv. 1 (7) (2020) 2163–2181.

[31] H. Zhang, X. Liu, Y. Wu, C. Guan, A.K. Cheetham, J. Wang, MOF-derived nanohybrids for electrocatalysis and energy storage: current status and perspectives, Chem. Commun. 54 (2018) 5268–5288.

[32] S.-K. Park, J.-S. Park, Y.C. Kang, Selenium-infiltrated metal–organic framework-derived porous carbon nanofibers comprising interconnected bimodal pores for Li–Se batteries with high capacity and rate performance, J. Mater. Chem. A 6 (3) (2018) 1028–1036.

[33] R. Liu, F. Guo, X. Zhang, J. Yang, M. Li, W. Miaomiao, H. Liu, M. Feng, L. Zhang, Novel "bird-nest" structured Co_3O_4/acidified multiwall carbon nanotube (ACNT) hosting materials for lithium–sulfur batteries, ACS Appl. Energy Mater. 2 (2) (2019) 1348–1356.

[34] Y.i. Jiang, H. Liu, X. Tan, L. Guo, J. Zhang, S. Liu, Y. Guo, J. Zhang, H. Wang, W. Chu, Monoclinic ZIF-8 nanosheet-derived 2D carbon nanosheets as sulfur immobilizer for high-performance lithium sulfur batteries, ACS Appl. Mater. Interfaces 9 (30) (2017) 25239–25249.

[35] Y. Liu, X. Qin, S. Zhang, G. Liang, F. Kang, G. Chen, B. Li, Fe_3O_4-decorated porous graphene interlayer for high-performance lithium–sulfur batteries, ACS Appl. Mater. Interfaces 10 (31) (2018) 26264–26273.

[36] Z. Li, Z. Xiao, S. Wang, Z. Cheng, P. Li, R. Wang, Engineered interfusion of hollow nitrogen-doped carbon nanospheres for improving electrochemical behavior and energy density of lithium–sulfur batteries, Adv. Funct. Mater. 29 (2019) 1902322.

[37] L. Fan, P. Sun, L.i. Yang, Z. Xu, J. Han, Facile and scalable synthesis of nitrogen-doped ordered mesoporous carbon for high performance supercapacitors, Korean J. Chem. Eng. 37 (1) (2020) 166–175.

[38] E. Lim, J. Chun, C. Jo, J. Hwang, Recent advances in the synthesis of mesoporous materials and their application to lithium-ion batteries and hybrid supercapacitors, Korean J. Chem. Eng. 38 (2) (2021) 227–247.

[39] A. Nulu, V. Nulu, K.Y. Sohn, Silicon and porous MWCNT composite as high capacity anode for lithium-ion batteries, Korean J. Chem. Eng. 37 (10) (2020) 1795–1802.

[40] P. Wang, R. Zeng, L. You, H. Tang, J. Zhong, S. Wang, T. Yang, J. Liu, Graphene-like matrix composites with Fe_2O_3 and Co_3O_4 as cathode materials for lithium–sulfur batteries, ACS Appl. Nano Mater. 3 (2020) 1382–1390.

[41] H. Ahn, Y. Kim, J. Bae, Y.K. Kim, W.B. Kim, A multifunctional SnO_2-nanowires/carbon composite interlayer for high-performance lithium-sulfur batteries, Chem. Eng. J. 401 (2020), 126042.

[42] W. Li, J. Hicks-Garner, J. Wang, J. Liu, A.F. Gross, E. Sherman, J. Graetz, J.J. Vajo, P. Liu, V_2O_5 polysulfide anion barrier for long-lived Li–S batteries, Chem. Mater. 26 (2014) 3403–3410.

[43] K. Kim, P.J.H. Kim, J.P. Youngblood, V.G. Pol, Surface functionalization of carbon architecture with nano-MnO_2 for effective polysulfide confinement in lithium–sulfur batteries, ChemSusChem 11 (2018) 2375–2381.

[44] J.S. Lee, R. Saroha, S.H. Oh, D.H. Shin, S.M. Jeong, J.K. Kim, J.S. Cho, Rational design of perforated bimetallic (Ni, Mo) sulfides/N-doped graphitic carbon composite microspheres as anode materials for superior Na-ion batteries, Small Methods 5 (2021) 2100195.

[45] L. Shen, Q. Che, H. Li, X. Zhang, Mesoporous $NiCo_2O_4$ nanowire arrays grown on carbon textiles as binder-free flexible electrodes for energy storage, Adv. Funct. Mater. 24 (2014) 2630–2637.

[46] Y.T. Liu, D.D. Han, L. Wang, G.R. Li, S. Liu, X.P. Gao, $NiCo_2O_4$ nanofibers as carbon-free sulfur immobilizer to fabricate sulfur-based composite with high volumetric capacity for lithium–sulfur battery, Adv. Energy Mater. 9 (2019) 1803477.

[47] Q.i. Fan, W. Liu, Z. Weng, Y. Sun, H. Wang, Ternary hybrid material for high-performance lithium–sulfur battery, J. Am. Chem. Soc. 137 (40) (2015) 12946–12953.

[48] S. Yang, N. Xia, M. Li, P. Liu, Y. Wang, L. Qu, Facile synthesis of a zeolitic imidazolate framework-8 with reduced graphene oxide hybrid material as an efficient electrocatalyst for nonenzymatic $_{H}2_{O}2$ sensing, RSC Adv. 9 (2019) 15217–15223.

[49] D. Wu, Z. Zou, X. Lu, K. Guo, N. Yang, C. Xu, 3D conductive NiCo/$NiCoO_x$ hybrid nanoclusters modified with amorphous FeOOH nanosheets for sensitive nonenzymatic glucose sensor, J. Mater. Sci. 54 (2019) 10695–10704.

[50] T.-H. Ko, K. Devarayan, M.-K. Seo, H.-Y. Kim, B.-S. Kim, Facile synthesis of core/shell-like $NiCo_2O_4$-decorated MWCNTs and its excellent electrocatalytic activity for methanol oxidation, Sci. Rep. 6 (2016) 1–9.

[51] M. Cheng, H. Fan, Y. Song, Y. Cui, R. Wang, Interconnected hierarchical $NiCo_2O_4$ microspheres as high-performance electrode materials for supercapacitors, Dalton Trans. 46 (2017) 9201–9209.

[52] X. Xiao, X. Zhang, Z. Zhang, J. You, S. Liu, Y. Wang, Macro-/meso-porous $NiCo_2O_4$ synthesized by template-free solution combustion to enhance the performance of a nonenzymatic amperometric glucose sensor, Microchim. Acta 187 (2020) 1–9.

[53] Y. Pan, W. Zeng, L. Li, Y. Zhang, Y. Dong, D. Cao, G. Wang, B.L. Lucht, K. Ye, K. Cheng, A facile synthesis of $ZnCo_2O_4$ nanocluster particles and the performance as anode materials for lithium ion batteries, Nano-Micro Lett. 9 (2017) 1–9.

[54] J. Pu, J. Wang, X. Jin, F. Cui, E. Sheng, Z. Wang, Porous hexagonal $NiCo_2O_4$ nanoplates as electrode materials for supercapacitors, Electrochim. Acta 106 (2013) 226–234.

[55] J.S. Lee, M.S. Jo, R. Saroha, D.S. Jung, Y.H. Seon, J.S. Lee, Y.C. Kang, D.W. Kang, J. S. Cho, Hierarchically well-developed porous graphene nanofibers comprising N-doped graphitic C-coated cobalt oxide hollow nanospheres as anodes for high-rate Li-ion batteries, Small 16 (2020) 2002213.

[56] S.H. Oh, S.M. Park, D.-W. Kang, Y.C. Kang, J.S. Cho, Fibrous network of highly integrated carbon nanotubes/MoO_3 composite bundles anchored with MoO_3 nanoplates for superior lithium ion battery anodes, J. Ind. Eng. Chem. 83 (2020) 438–448.

[57] V. Venkatachalam, A. Alsalme, A. Alghamdi, R. Jayavel, Hexagonal-like $NiCo_2O_4$ nanostructure based high-performance supercapacitor electrodes, Ionics 23 (2017) 977–984.

[58] R. Saroha, A.K. Panwar, Effect of *in situ* pyrolysis of acetylene (C_2H_2) gas as a carbon source on the electrochemical performance of $LiFePO_4$ for rechargeable lithium-ion batteries, J. Phys. D: Appl. Phys. 50 (2017), 255501.

[59] C. Luo, E. Hu, K.J. Gaskell, X. Fan, T. Gao, C. Cui, S. Ghose, X.-Q. Yang, C. Wang, A chemically stabilized sulfur cathode for lean electrolyte lithium sulfur batteries, Proc. Nat. Acad. Sci. 117 (26) (2020) 14712–14720.

[60] K. Sun, H. Liu, H. Gan, Cathode loading effect on sulfur utilization in lithium–sulfur battery, J. Electrochem. Energy Convers. Storage 13 (2016), 021002.

[61] X. Guo, K. Li, W. Bao, Y. Zhao, J. Xu, H. Liu, G. Wang, Highly reversible lithium polysulfide semiliquid battery with nitrogen-rich carbon fiber electrodes, Energy Technol. 6 (2) (2018) 251–256.

[62] Y. Li, S. Yao, C. Zhang, Y. He, Y. Wang, Y. Liang, X. Shen, T. Li, S. Qin, W. Wen, Molybdenum carbide nanocrystals modified carbon nanofibers as electrocatalyst for enhancing polysulfides redox reactions in lithium-sulfur batteries, Int. J. Energy Res. 44 (11) (2020) 8388–8398.

[63] X. Zhang, C. Shang, E.M. Akinoglu, X. Wang, G. Zhou, Constructing Co_3S_4 nanosheets coating N-doped carbon nanofibers as freestanding sulfur host for high-performance lithium–sulfur batteries, Adv. Sci. 7 (2020) 2002037.

[64] S. Yao, S. Xue, S. Peng, M. Jing, X. Shen, T. Li, Z. YiLiu, Electrospun zeolitic imidazolate framework-derived nitrogen-doped carbon nanofibers with high performance for lithium-sulfur batteries, Int. J. Energy Res. 43 (5) (2019) 1892–1902.

[65] J. Wang, Y. Li, W. Li, C. Sun, C. Qi, J. Jin, Z. Wen, Multiple nanosheets assembled nanoflower-like MnO_2 to anchor polysulfides for improving electrochemical performance in lithium sulfur batteries, ChemistrySelect 4 (24) (2019) 7102–7107.

[66] L. Luo, S.-H. Chung, A. Manthiram, A three-dimensional self-assembled SnS_2-nano-dots@graphene hybrid aerogel as an efficient polysulfide reservoir for high-performance lithium–sulfur batteries, J. Mater. Chem. A 6 (17) (2018) 7659–7667.

[67] H. Xu, A. Manthiram, Hollow cobalt sulfide polyhedra-enabled long-life, high areal-capacity lithium-sulfur batteries, Nano Energy 33 (2017) 124–129.

[68] D.-H. Lim, M. Agostini, F. Nitze, J. Manuel, J.-H. Ahn, A. Matic, Route to sustainable lithium-sulfur batteries with high practical capacity through a fluorine free polysulfide catholyte and self-standing carbon nanofiber membranes, Sci. Rep. 7 (2017) 1–9.

[69] C.-H. Chang, S.-H. Chung, A. Manthiram, Highly flexible, freestanding tandem sulfur cathodes for foldable Li–S batteries with a high areal capacity, Mater. Horiz. 4 (2) (2017) 249–258.

[70] S.-H. Chung, A. Manthiram, Carbonized eggshell membrane as a natural polysulfide reservoir for highly reversible Li-S batteries, Adv. Mater. 26 (9) (2014) 1360–1365.

[71] X. Pu, G. Yang, C. Yu, Trapping polysulfides catholyte in carbon nanofiber sponges for improving the performances of sulfur batteries, J. Electrochem. Soc. 162 (7) (2015) A1396.

[72] X. Pu, G. Yang, C. Yu, Liquid-type cathode enabled by 3D sponge-like carbon nanotubes for high energy density and long cycling life of Li-S batteries, Adv. Mater. 26 (44) (2014) 7456–7461.

[73] C. Cavallo, M. Agostini, J.P. Genders, M.E. Abdelhamid, A. Matic, A free-standing reduced graphene oxide aerogel as supporting electrode in a fluorine-free Li_2S_8 catholyte Li-S battery, J. Power Sources 416 (2019) 111–117.

[74] X. Li, X. Pu, S. Han, M. Liu, C. Du, C. Jiang, X. Huang, T. Liu, W. Hu, Enhanced performances of Li/polysulfide batteries with 3D reduced graphene oxide/carbon nanotube hybrid aerogel as the polysulfide host, Nano Energy 30 (2016) 193–199.

[75] Y. Fu, Y.-S. Su, A. Manthiram, Highly reversible lithium/dissolved polysulfide batteries with carbon nanotube electrodes, Angew. Chem. Int. Ed. 52 (27) (2013) 6930–6935.

[76] X. Hong, J. Jin, T. Wu, Y. Lu, S. Zhang, C. Chen, Z. Wen, A rGO–CNT aerogel covalently bonded with a nitrogen-rich polymer as a polysulfide adsorptive cathode for high sulfur loading lithium sulfur batteries, J. Mater. Chem. A 5 (28) (2017) 14775–14782.

[77] S. Huang, Y.e. Wang, J. Hu, Y.V. Lim, D. Kong, Y. Zheng, M. Ding, M.E. Pam, H. Y. Yang, Mechanism investigation of high-performance Li–polysulfide batteries enabled by tungsten disulfide nanopetals, ACS Nano 12 (9) (2018) 9504–9512.

[78] K. Han, J. Shen, S. Hao, H. Ye, C. Wolverton, M.C. Kung, H.H. Kung, Free-standing nitrogen-doped graphene paper as electrodes for high-performance lithium/dissolved polysulfide batteries, ChemSusChem 7 (9) (2014) 2545–2553.

[79] D. Fang, Y. Wang, C. Qian, X. Liu, X. Wang, S. Chen, S. Zhang, Synergistic regulation of polysulfides conversion and deposition by MOF-derived hierarchically ordered carbonaceous composite for high-energy lithium–sulfur batteries, Adv. Funct. Mater. 29 (2019) 1900875.

[80] J.W. Kim, G. Seo, S. Bong, J. Lee, Improved redox reaction of lithium polysulfides on the interfacial boundary of polar CoC_2O_4 as a polysulfide catenator for a high-capacity lithium-sulfur battery, ChemSusChem 14 (3) (2021) 876–883.

[81] X. Liang, C. Hart, Q. Pang, A. Garsuch, T. Weiss, L.F. Nazar, A highly efficient polysulfide mediator for lithium–sulfur batteries, Nat. Commun. 6 (2015) 1–8.

[82] R. Saroha, J. Heo, Y. Liu, N. Angulakshmi, Y. Lee, K.-K. Cho, H.-J. Ahn, J.-H. Ahn, V_2O_3-decorated carbon nanofibers as a robust interlayer for long-lived, high-performance, room-temperature sodium–sulfur batteries, Chem. Eng. J. 431 (2022), 134205.